DNS of heat transfer from a cylinder immersed in the production and decay regions of grid-element turbulence

I.Paul†, G.Papadakis†, and J.C.Vassilicos†

Department of Aeronautics, Imperial College London, London - SW7 2AZ, UK

The present DNS study, the first of its kind, explores the effect that the location of a cylinder, immersed in the turbulent wake of a grid-element, has on heat transfer. An insulated single square grid-element is used to generate the turbulent wake upstream of the heated circular cylinder. Due to fine-scale resolution requirements, the simulations are carried out for a low Reynolds number. Three locations downstream of the grid-element, inside the production, peak and decay regions, respectively are considered. The turbulent flow in the production and peak regions is highly intermittent, non-Gaussian and inhomogeneous, while it is Gaussian, homogeneous, and fully-turbulent in the decay region. The turbulence intensities at the location of the cylinder in the production and decay regions are almost equal at 11%, while the peak location has the highest turbulent intensity of 15%. A baseline simulation of heat transfer from the cylinder without oncoming turbulence was also performed. Although the oncoming turbulent intensities are similar, the production region increases the stagnation point heat transfer by 63%, while in the decay region it is enhanced by only 28%. This difference cannot be explained only by the increased approaching velocity in the production region. The existing correlations for the stagnation point heat transfer coefficient are found invalid for the production and peak locations, while they are satisfied in the decay region. It is established that the flow in the production and peak regions is dominated by shedding events, in which the predominant vorticity component is in the azimuthal direction. This leads to increased heat transfer from the cylinder, even before vorticity is stretched by the accelerating boundary layer. The frequency of oncoming turbulence in production and peak cases also lies close to the range of frequencies that can penetrate the boundary layer developing on the cylinder, and therefore the latter is very responsive to the impinging disturbances. The highest Nusselt number along the circumference of the cylinder is shifted 45 degrees from the front stagnation point. This shift is due to the turbulence-generating grid-element bars that result in the prevalence of intense events at the point of maximum Nusselt number compared to the stagnation point.

1. Introduction

Free-stream turbulence impinging on a surface aids the transition of developing laminar boundary layer (Zdravkovich 1997). When the surface is exposed to heat, the boundary layer transition is expected to impact the heat transfer. Interestingly, experiments have revealed that heat transfer increases not only in the turbulent part, but a substantial amount also occurs even in places where the boundary layer is still laminar (Dullenkopf & Mayle 1994, 1995). Such an observation are also seen in the turbine blades of an aircraft

† Email addresses for correspondence: p.immanuvel@imperial.ac.uk, g.papadakis@imperial.ac.uk, j.c.vassilicos@imperial.ac.uk

engine which are exposed to hot gases. The heat load on the turbine blades is increased due to the free-stream turbulence coming from the combustion chamber as well as the preceding blade rows. Although the entire pressure surface and most of the suction surface of the blade remain laminar upon being exposed to free-stream turbulence, these regions exhibit enhanced heat transfer (Dullenkopf & Mayle 1994, 1995). The effect of free-stream turbulence on heat transfer through a laminar boundary layer is termed 'laminar heat transfer' (Dullenkopf & Mayle 1994, 1995). Understanding the characteristics of free-stream turbulence, and their effect on the laminar heat transfer is of paramount importance, for instance, in designing a better turbine blade cooling system. The laminar heat transfer scenario can also be observed at the stagnation point of more simplified geometries, such as the circular cylinder.

1.1. *Literature on heat transfer due to free-stream turbulence*

While there are numerous experimental studies available on the subject of laminar heat transfer, only a few theoretical and numerical studies can be found. These studies are briefly discussed below under three broad categories (i) primary factors affecting laminar heat transfer, (ii) stagnation point heat transfer coefficient correlations, and (iii) heat transfer enhancement mechanism.

1.1.1. *Primary factors affecting laminar heat transfer*

The literature reveals that the primary factors affecting heat transfer through a laminar boundary layer are (i) straining by the mean flow (a), (ii) turbulent intensity (Tu), (iii) Reynolds number (Re), and (iv) turbulence length scale (L_u). Secondary factors such as the cylinder blockage, surface roughness, thermal boundary condition, Prandtl number etc can also influence the heat transfer, but they are not widely considered in the literature.

Early experiments conducted on flow over a flat plate established the effect of mean flow straining (Kestin *et al.* 1961; Junkhan & Serovy 1967). These experiments were carried out for various combinations of turbulent intensity and pressure gradient. Increase of turbulent intensity did not enhance the laminar heat transfer when the pressure gradient was zero. On the other hand, increase in turbulent intensity resulted in increased heat transfer when a favorable pressure gradient was present. As a result, these studies concluded that, in order for the free-stream fluctuations to have an effect on the laminar heat transfer, the flow must be accelerating.

Almost all of the existing experiments in the literature report that the laminar heat transfer in an accelerating flow increases for increasing turbulent intensity and Reynolds number (Kestin *et al.* 1961; Junkhan & Serovy 1967; VanFossen & Simoneau 1987; Dullenkopf *et al.* 1990; Paxson & Mayle 1991; Liu & Rodi 1994; Magari & LaGraff 1994; Ames 1995; Ames *et al.* 2002; Chowdhury & Ames 2013; Kingery & Ames 2016). Note that the flow configurations of these experiments are very diverse, ranging from flat plates, airfoils, cylinders to rows of airfoils.

The study of Yardi & Sukhatme (1978) provided the first experimental evidence for the importance of turbulence length scales in laminar heat transfer. A turbulence length scale of 4 to 12 times the laminar boundary layer thickness produced the highest heat transfer increase. Length scales below and above this range had a smaller effect. Their observation was later verified in various experimental studies (Van Fossen *et al.* 1995; Lowery & Vachon 1975; Ames 1991). A similar result was derived in the theoretical study of Xiong & Lele (2004).

To the best of the authors' knowledge, only a handful of numerical studies are available in the literature on the subject of laminar heat transfer (Wissink & Rodi 2006, 2009;

Xiong & Lele 2007; Bhaskaran & Lele 2010; Wissink & Rodi 2011*a*,*b*; Venema *et al.* 2011, 2014). The studies of Xiong & Lele (2007) and Bhaskaran & Lele (2010) are large eddy simulations (LES), while the studies of Venema *et al.* (2011, 2014) are semi Direct Numerical Simulations (DNS), in the sense that the turbulence generating body is not fully resolved. A collective conclusion from these studies is that the observations noted by the experiments were indeed reproduced numerically as well.

1.1.2. *Stagnation point heat transfer correlations*

The second group of studies focused on obtaining a functional relationship for the stagnation point mean *Nusselt* number, $\langle Nu \rangle_0$, where $\langle Nu \rangle = \frac{q_w D}{\langle T_w^* - T_\infty^* \rangle}$, q_w is the amount of heat-flux applied on the cylinder, D is the diameter of the cylinder, T_w^* and T_∞^* are the temperatures at the wall and free-stream respectively. Earlier studies attempted to correlate $\langle Nu \rangle_0$ with the mean flow straining, Reynolds number and turbulent intensity, while omitting the turbulence length scale (Kestin *et al.* 1961; Lowery & Vachon 1975). The most successful correlation was obtained by Dullenkopf & Mayle (1994):

$$Nu_a Pr^{-0.37} = 0.571 + 0.0125 Tu_a \left(1 + \frac{1.8}{1 + (Tu_a/20)^3}\right) \tag{1.1}$$

where Nu_a is the modified Nusselt number $Nu_a = \langle Nu \rangle_0 / \sqrt{a_1 Re_{inc}}$, and Tu_a is a modified turbulent intensity $Tu_a = Tu \sqrt{Re_{inc}/a_1}$. In these definitions, $Re_{inc} = U_{inc}D/\nu$, where U_{inc} is the incident velocity and ν is the kinematic viscosity. The normalised free-stream straining is denoted as $a_1 = aD/U_{inc}$, where 'a' is the free-stream mean straining of the flow.

Although equation (1.1) was observed to give a better collapse of available heat transfer experimental data at large turbulent intensities, there was still a scatter of data for low intensity values. This scatter was later reduced in the study of Dullenkopf & Mayle (1995) where the effect of turbulence length scale was also included. Denoting the modified length scale as $L_a = \frac{L_u}{D}\sqrt{a_1 Re_{inc}}$, the new correlation is written as:

$$Nu_a Pr^{-0.37} = 0.571 + 0.01 Tu_\lambda \tag{1.2}$$

where Tu_λ is a turbulence parameter defined as,

$$Tu_\lambda = \frac{Tu_a \sqrt{L_a}}{(1 + 0.004 L_a^2)^{5/12}} \tag{1.3}$$

The constants in equations (1.1) and (1.2) are obtained from curve fitting. The correlations (1.1) and (1.2) are presently widely accepted. Their validity was assessed in the numerical studies of Wissink & Rodi (2011*a*,*b*); Venema *et al.* (2011, 2014), and was found to be satisfactory.

1.1.3. *Mechanism of heat transfer enhancement*

The third group of studies investigated the heat transfer enhancement mechanism. Although it is known from the study of Kestin *et al.* (1961) that the primary reason for heat transfer is the mean straining of the flow, the complete mechanism can be obtained from rapid distortion theory (refer to Hunt (1973)). Small-scale eddies increase heat transfer upon being stretched by the mean accelerating boundary layer due to the amplification of their turbulent intensity. This effect is felt up to three radii from the centre of the cylinder. The large scale eddies are blocked by the boundary layer, and this effect is felt up to one integral length scale from the surface of the cylinder.

Most of the experimental studies provided validation of this mechanism only by checking if the boundary layer is accelerating or not as they were limited to measure

only one point statistics. Yet, the experimental study of Hubble *et al.* (2013) provided an elegant picture of the role of vortical structures in stagnation heat transfer enhancement. In particular, they observed that the oncoming vortical structure has little impact on heat transfer when it is far off from the surface. As the vortex approaches near the surface, its vorticity and circulation is enhanced and this vortex indulges in heat transfer enhancement through sweeping cold fluid towards the surface.

Numerical studies also have painted a better picture of this mechanism. For example, the DNS studies of Wissink & Rodi (2006), Wissink & Rodi (2009, 2011*a*) showed that the increase in heat transfer occurs through an up-wash of hot fluid away from the cylinder and a down-wash of cold fluid towards the cylinder. The LES studies of Xiong & Lele (2007) and Bhaskaran & Lele (2010) observed longitudinal stream-wise vortical structures that increase heat transfer by being stretched along the surface of the turbine blade.

1.2. *The research gap and present investigation*

Almost all of the experimental studies found in the literature on laminar heat transfer have used a classical grid to generate the oncoming turbulence. In a few studies the turbulence generator was in the form of a circular cylinder. Yet, all these studies are similar in one particular aspect: the oncoming turbulence was always observed to be homogeneous, *Gaussian* and fully-turbulent.

Recently there has been increased interest in turbulence generated by fractal grids. Following the work of Seoud & Vassilicos (2007), many studies have focused on the turbulent flow generated by multi-scale or fractal grids (Mazellier & Vassilicos 2010; Valente & Vassilicos 2011; Gomes-Fernandes *et al.* 2012). In these flows, an extended production region exists immediately downstream of the grid, besides the usual decay region far downstream. The production region is characterised by increasing turbulent intensity, while in the decay region the turbulence intensity decreases. Even though the decay region is close to homogeneous and *Gaussian*, the dissipation coefficient of turbulent kinetic energy is not constant. This non-equilibrium scaling of dissipation is reviewed by Vassilicos (2015). Recent DNS studies have revealed that the fractal grid turbulence characteristics can also be observed behind the square grid-element i.e. the largest scale feature of a fractal grid without fractal iterations (Zhou *et al.* 2014, 2016*a*,*b*; Paul *et al.* 2017). In particular, the production region behind the grid-element is found to be inhomogeneous and non-Gaussian, similar to that of the fractal grid turbulence. The effect of developing inhomogeneous turbulence on heat transfer has not been considered in the literature. Consequently, the following questions arise:

(i) What is the effect of different regions such as the production, peak and decay, on the heat transfer characteristics?

(ii) Are the existing correlations for the stagnation point heat transfer coefficient valid for a developing intermittent turbulence?

(iii) How does heat transfer enhancement happen when the oncoming turbulence characteristics are different from the one reported in the literature?

This paper aims to answer the aforementioned questions by considering the effect of free-stream turbulence on heat transfer from a circular cylinder. A square grid-element is used to generate the oncoming free-stream turbulence. In order to study the effect of turbulence, the grid-element is insulated (i.e. adiabatic) while the circular cylinder is heated. The cylinder is placed at three distinct locations in the wake of the grid-element. These locations are carefully chosen such that the production and decay regions have the same turbulent intensity.

The rest of this paper is structured as follows. Section 2 highlights the numerical

challenges associated with studying the current configuration before presenting details of the numerical setup and boundary conditions. The characteristics of oncoming turbulence are discussed in §3 in terms of velocity, rms profiles, and statistical measures such as skewness and flatness. The intermittent nature of the oncoming flow is also properly characterised in the same section. This is followed by analysis of the effects of free-stream turbulence on flow and thermal characteristics on the surface of the cylinder in §4 and §5 respectively. Section 6 assesses the validity of the existing stagnation point heat transfer coefficient correlations, and they are found to be invalid in the production and peak regions. The following sections (§7 and §8) provide explanations as to why these correlations are not valid. This includes an analysis of the dominant frequency of turbulent fluctuations and a timescale analysis. The physical mechanism responsible for heat transfer increase is also identified and explained for each region in §8. Finally, the results of this DNS are compared with high Reynolds numbers experiments in §9; similarities and differences are identified and explained.

2. Computational details

2.1. *Numerical method*

Throughout this paper, instantaneous, mean, and fluctuating velocity fields are denoted as u_i^*, U_i, and u_i respectively (where $i = 1, 2, 3$), and the corresponding variables for pressure and temperature are p^*, P, p and T^*, $\langle T \rangle$, T respectively. Close to the cylinder, the velocity vector is decomposed into radial, azimuthal, and spanwise components which are represented with the subscripts r, θ, and z respectively. Following the above notation, the instantaneous velocities are represented as u_r^*, u_θ^*, u_z^*, the mean velocities as U_r, U_θ, U_z and the fluctuating components as u_r, u_θ and u_z. The continuity, momentum and temperature conservation equations are written for an incompressible flow as:

$$\frac{\partial u_i^*}{\partial x_i} = 0 \tag{2.1}$$

$$\frac{\partial u_i^*}{\partial t} + u_j^* \frac{\partial u_i^*}{\partial x_j} = -\frac{1}{\rho}\frac{\partial p^*}{\partial x_i} + \nu \frac{\partial^2 u_i^*}{\partial x_j \partial x_j} \tag{2.2}$$

$$\frac{\partial T^*}{\partial t} + u_j^* \frac{\partial T^*}{\partial x_j} = \alpha \frac{\partial^2 T^*}{\partial x_j \partial x_j} \tag{2.3}$$

where ρ, ν, and α are the density, kinematic viscosity and thermal diffusivity respectively.

These governing equations are solved using an in-house parallel code named '*Pantarhei*'. It is an unstructured finite volume solver in collocated variable arrangement. The convective and diffusion terms are discretized by a second-order central differencing scheme, while the transient term is discretised by a second-order backward scheme. The code is parallelised using the PETSc libraries (Balay *et al.* 2014). Details of the solver have been reported in previous studies (Paul *et al.* 2017; Paul 2017; Paul *et al.* 2018), and are not repeated here.

2.2. *Numerical challenges*

This study presents DNS results of heat transfer from a circular cylinder immersed in the turbulent wake generated by a single square grid-element. A study of this kind is numerically challenging due to several factors. Firstly, the surfaces of the grid-element require fine resolution to capture the correct dynamics of the turbulent flow it generates,
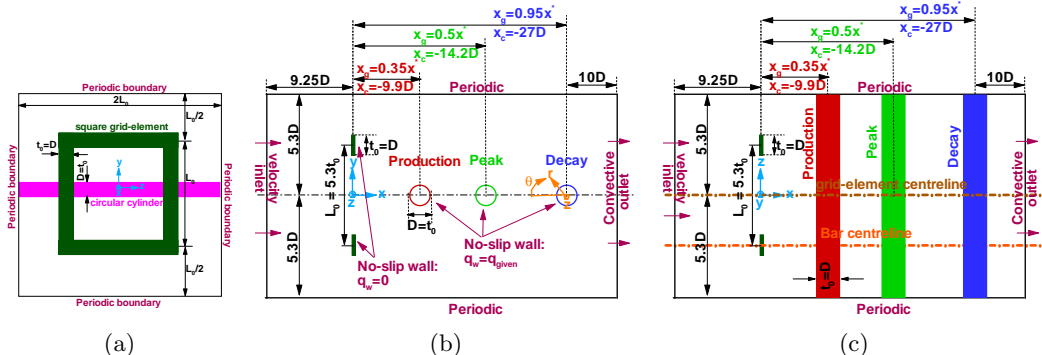
(a)   (b)   (c)

Figure 1: Sketch of the computational domain: (a) front view, (b) sectional view at the plane z/D=0, (c) sectional view at the plane y/D=0. (The sketches are not to scale).

while the flow close to the surface of the cylinder also has to be resolved well in order to predict the correct heat transfer. Such requirements increase the number of cells significantly, in particular for high Reynolds numbers. To the best of authors' knowledge, only the semi-DNS studies of Venema *et al.* (2011, 2014) included the turbulence-generating body in the computational domain. Nonetheless, the flow around the body was not fully resolved and these studies are, therefore, only semi-DNS studies. In the studies of Wissink & Rodi (2011*a,b*), the inlet fluctuations were obtained from a separate precursor simulation.

Secondly, the spanwise length of the grid-element is larger compared to the standard spanwise size used to compute the flow around a single cylinder. For example, the study of Venema *et al.* (2011) had a spanwise length of 2.5D, while Wissink & Rodi (2011*b*) and Wissink & Rodi (2011*a*) had 2D and 0.6D respectively. The presence of the grid-element increases this size by a factor of 7, which in turn increases the number of cells accordingly.

Thirdly, in our study the distance between the cylinder and the turbulence-generating body is larger than the typical distances used in previous works. In Wissink & Rodi (2011*b,a*) this distance is usually set to less than 2D, but in the present study the cylinder is up to a maximum of $27D$ from the turbulence-generating body. This increases the number of computational cells substantially.

Taking these factors into consideration, simulating heat transfer from a cylinder in the presence of a grid-element, even at a moderate Reynolds number, requires a large number of cells. As shown in Paul *et al.* (2017), the turbulence generated by a single square element shares many similarities with the turbulence generated by regular or fractal grids. A regular or fractal grid will increase the complexities of the simulation as they have a larger wetted-area compared to the grid-element. Due to these reasons, this work explores the effect of turbulence generated by a single square grid-element.

2.3. *Simulation setup*

The front view of the computational domain is shown in figure 1a where the dimensions of the grid-element and the cylinder are noted. The square grid-element has a lateral thickness of t_0=43mm, a length of $L_0 = 5.3t_0 = 229$mm, and a streamwise thickness of $0.14t_0 \approx 6$mm. Thus, the aspect ratio (defined as the ratio between streamwise to lateral thickness) of the grid-element is 0.14, and not 1.0 as in the case of classical grids. We have

chosen this aspect ratio because we also want to compare with fractal grid turbulence experiments of Melina *et al.* (2017). Since the fractal grid has a streamwise thickness equal to the thickness of the smallest grid-element, the streamwise thickness of the current grid-element is $6mm$. The effect of grid-element aspect ratio on turbulence dynamics has already been addressed in Paul *et al.* (2017).

The diameter of the cylinder (D) is equal to the lateral thickness of the grid-element bar, i.e. $D = t_0$. The side view of the computational domain (figure 1b) shows that the square grid-element is placed at a distance $9.25D$ from the inlet. The size of the computational domain in the cross-streamwise and spanwise directions is $2L_0 \times 2L_0$. The distance between the cylinder and the outlet is kept constant at $10D$ for all simulations. The dimensions of our computational domain are taken from the experiments of Melina *et al.* (2017).

For this simulation setup, two different variables and their corresponding length scales are used to represent the streamwise distance. The variable x_g is used to represent the streamwise distance with origin at the grid-element as shown in figure 1b. On the other hand, the variable x_c, with its origin at the centroid of the cylinder (see the polar coordinates in figure 1b), is used to represent the streamwise distance with respect to the cylinder centre. A wake-interaction length scale, defined as $x^* = L_0^2/t_0$, is used to normalise x_g. The diameter of the cylinder, D, is used to normalise x_c.

As mentioned earlier, the cylinder is placed at three different locations downstream of the turbulence-generating grid-element. The terminology of these simulations is based on the turbulent kinetic energy evolution along the grid-element centreline as shown in figure 21a: it increases for $x_g/x^* < 0.5$ (production region), it attains its maximum value around $x_g \approx 0.5x^*$ (peak region) and decreases for $x_g/x^* > 0.5$ (decay region). Accordingly, the simulations are termed '*Production*','*Peak*' and '*Decay*' and the cylinder is placed at $x_g = 0.35x^*$, $0.5x^*$ and $0.95x^*$ respectively. The locations are carefully chosen so as to have similar oncoming turbulent intensity values for the 'production' and 'decay' simulations, while the simulation 'peak' has the highest turbulent intensity value. Behind the bars of the grid-element, the turbulent kinetic energy decays monotonically (see figure 21a).

The Reynolds number based on the inlet velocity and diameter of the cylinder (or the thickness of the grid-element) is $Re_D = U_\infty D/\nu = Re_{t_0} = U_\infty t_0/\nu = 500$. The blockage ratio for the grid-element is 20%, while for the cylinder is approximately 10%. The details of these simulations are documented in table 1. The Prandtl number (defined as $Pr = \nu/\alpha$) is always 0.71.

We have performed also two baseline simulations. The first simulation is the flow past the grid-element without a cylinder. The Reynolds number Re_{t_0} is 500. This simulation is termed '*grid − element*' and the details were already reported in Paul *et al.* (2017). The second baseline simulation is the heat transfer for a single cylinder at $Re_D = 500$ with steady approaching flow (no oncoming turbulence) and this simulation is termed '*Cylinder*'.

2.4. *Boundary conditions and computational mesh details*

Uniform velocity and temperature profiles are prescribed at the inlet and a convective boundary condition at the outlet. No-slip condition is applied on all solid surfaces. The grid-element is insulated (corresponding to zero heat-flux), while a uniform heat-flux is imposed on the cylinder. All lateral boundaries are periodic.

The mesh resolution for the grid-element is the same as the one reported in Paul *et al.* (2017). The turbulence generated is resolved up to the order of Kolmogorov length scale. The cross-sectional view of the mesh around the cylinder is shown in figure 2a. An O-type
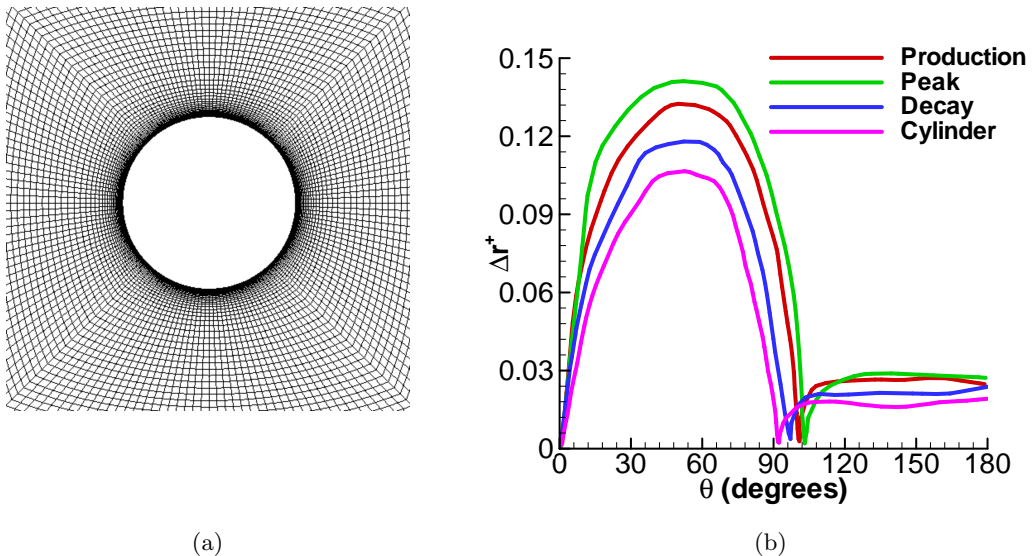
Figure 2: (a) Sectional view of an O-type mesh around the cylinder. (b) Variation of Δr^+ of the first grid point in the radial direction.

Simulation name	Maximum $\Delta\theta^+$	Maximum Δz^+	Number of cells	Re_{inc}	Tu
Production	0.12	0.08	18.7×10^6	600	11%
Peak	0.14	0.12	29.31×10^6	550	15%
Decay	0.11	0.09	48.5×10^6	500	11%
Cylinder	0.08	0.05	8.1×10^6	500	0
Grid-element	0.15 (Δn^+)	0.15 (Δn^+)	20.4×10^6	–	–

Table 1: Details of the simulations.

mesh is used which allows for fine resolution of boundary layers. Figure 2b quantifies the resolution of the mesh in terms of wall units along the circumference of the cylinder. This figure illustrates that the boundary layer is well-resolved, as the radial distance between the wall and the nearest mesh point is always less than 0.15 wall units. Mesh details for all simulations can be found in table 1. Every case is simulated approximated for 15 flow-through times or 250 vortex shedding cycles. This shows that our simulation has been run for much longer time than the previous DNS studies (Wissink & Rodi 2006, 2009).

2.5. *Validation*

We validate our DNS solver for flow around the grid-element as well as the cylinder. The validations pertaining to the grid-element are presented later when characterising
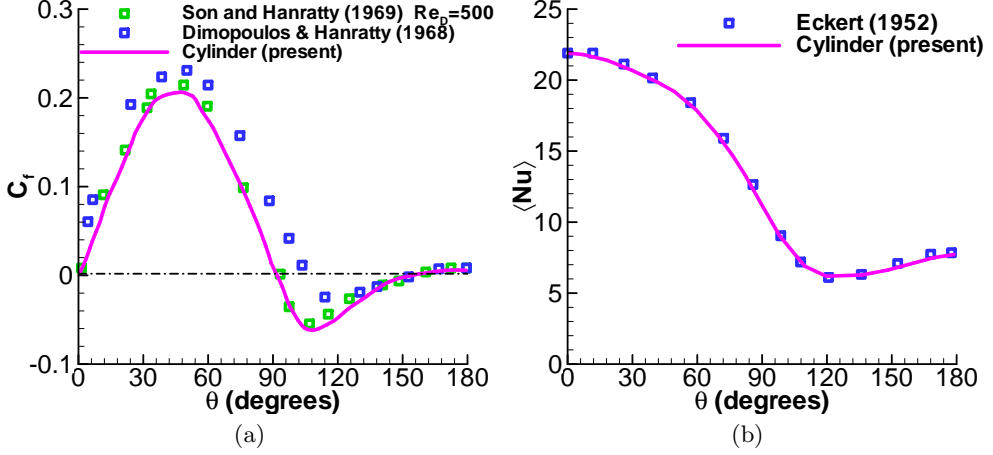
Figure 3: (a) Comparison of the skin-friction coefficient with the literature. The data for Re_D=339 is taken from Dimopoulos & Hanratty (1968), and for Re_D=500 is from Son & Hanratty (1969), (b) Comparison of mean Nusselt number variation with the experiments of Eckert (1952).

the oncoming turbulence. There is a lack of detailed reference data for the flow around the cylinder at Re_D=500. Since this study deals with near-wall phenomena, in figure 3 we present results for the skin-friction coefficient ($C_f = (\nu \partial U_\theta / \partial r)/U_\infty^2$) and the time-averaged Nusselt number ($\langle Nu \rangle$). The variation of C_f along the circumference of the cylinder, shown in figure 3a, is in good agreement with the experimental study of Dimopoulos & Hanratty (1968). Zdravkovich (1997) reports that the mean separation angle for $Re_D = 500$ is around 90°, and our study also produces a similar result. The time-averaged Nusselt number, shown in figure 3b, is also found to be in good agreement with the experiment of Eckert (1952).

Krall & Eckert (1973) proposed correlations for the stagnation point Nusselt number ($\langle Nu \rangle_0$), and for the overall Nusselt number ($\langle Nu \rangle_{overall}$, which is the circumferential average of $\langle Nu \rangle$). They are given as: $\langle Nu_0 \rangle$=0.95$Re_D^{0.5}$, and $\langle Nu_{overall} \rangle$=0.43+0.48$Re_D^{0.5}$. The $\langle Nu_0 \rangle$ and $\langle Nu_{overall} \rangle$ are 21.9 and 11.5 respectively, and their percentage error with respect to the correlations of Krall & Eckert (1973) for Re_D=500 are 1.6% and 3.19% respectively.

This validation provides evidence that the numerical mesh resolution employed in this study is adequate to compute the correct near-wall parameters of fluid flow and heat transfer.

3. Characteristics of oncoming turbulence

This study focuses only on the $x - y$ centre plane at z/D=0 (see figure 1b) for two reasons. Firstly, as shown in Paul *et al.* (2017), in this plane the oncoming flow is strongly inhomogenous and non-Gaussian. Secondly, as shown later in this paper, the stagnation point heat transfer coefficient correlations are not valid along the grid-element centreline in this plane.

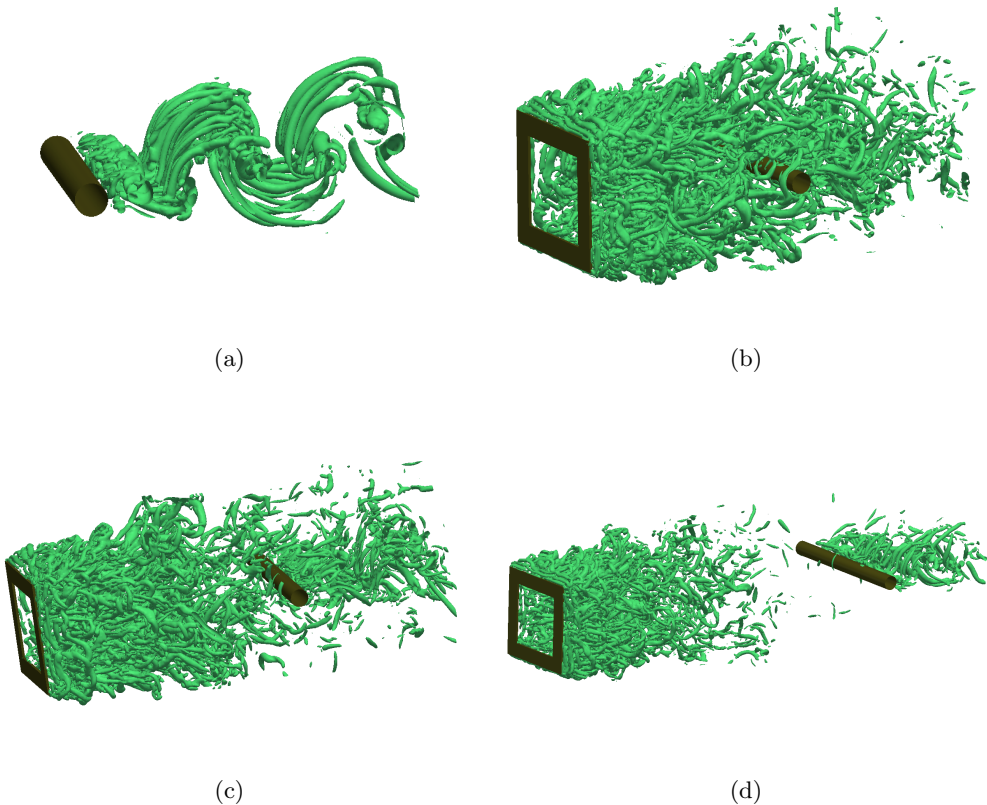Typical instantaneous flow fields are visualised in terms of iso-surfaces of Q-criterion in

Figure 4: Visualisation of turbulent coherent structures through iso-surfaces of the second invariant of the fluctuating velocity gradient tensor $(Q/(U_\infty/D)^2=3)$: (a) Circular, (b) Production, (c) Peak, (d) Decay.

figure 4. The turbulent flow from the grid-element has a wider range of scales compared to that of flow past the cylinder at this Reynolds number. This section is devoted to the characterisation of the oncoming turbulence generated by the single square grid-element.

3.1. *Mean and rms velocity profiles*

Mean velocity profiles along the centreline of the grid-element are shown in figure 5a for all the cases considered. The values are normalised by the free-stream velocity (U_∞). The approaching flow reaches zero at the streamwise location where the cylinder is placed due to the no-slip boundary condition. The velocity profiles are indistinguishable for $x_g/x^* < 0.2$. The velocity profile exhibits a jet-like behaviour close to the grid-element, followed by a monotonic decrease further downstream. Such a mean velocity variation implies that the incident Reynolds number near the cylinder is not the same as the inlet Reynolds number. The former is defined in terms of the incident velocity (U_{inc}) outside the boundary layer. In the cases considered, this is measured at x_c/D=-1.5, as this location is well outside the boundary layer, and the mean and rms velocities do not vary significantly as seen in figures 5b and 6b respectively. As expected, the incident mean velocity for the production case is the largest due to the jet-like behaviour. The incident velocities of the decay and the cylinder cases are almost equal. The computed incident Reynolds numbers
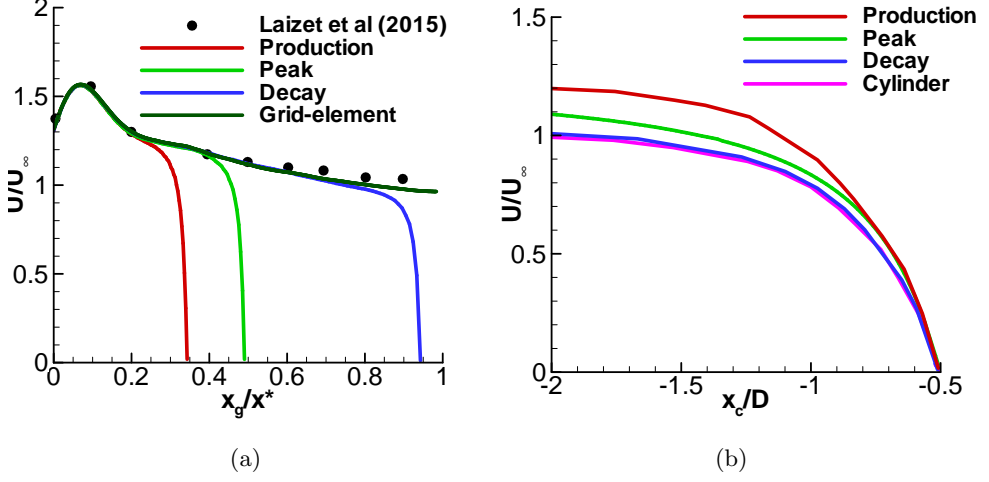
Figure 5: (a) Variation of mean velocity along the grid-element centreline, (b) Mean velocity profiles upstream of the cylinder in the plane $z/D=0$. Note the different horizontal axes in (a) and (b).
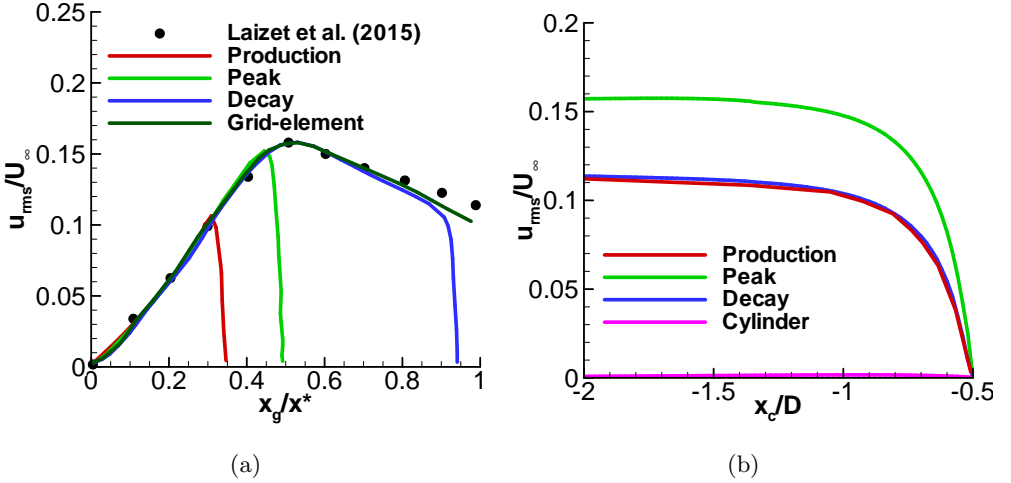

Figure 6: (a) Variation of rms velocity along the grid-element centreline, (b) Rms velocity profiles upstream of the cylinder in the plane $z/D=0$. Note the different horizontal axes in (a) and (b)

($Re_{inc}=U_{inc}D/\nu$) are documented in table 1. The mean velocity profiles in figure 5a are also compared against the experimental results of Laizet *et al.* (2015), and the matching is good. This provides the first evidence that the mesh resolution downstream of the grid-element is similar to the mesh used in Paul *et al.* (2017), and the grid-element and its wake are properly resolved.
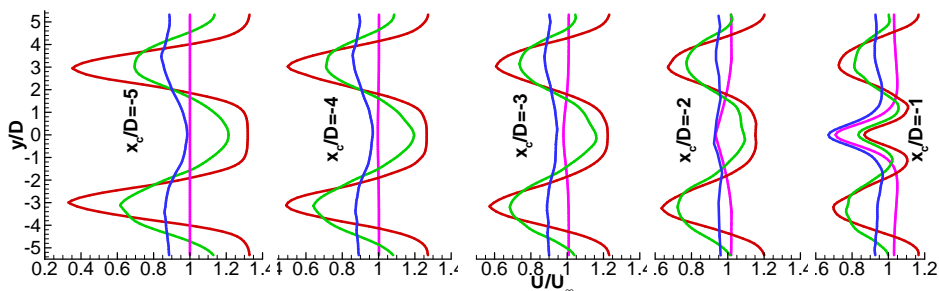
Figure 7: Development of mean velocity profiles upstream of the cylinder in the plane $z/D = 0$ (red - Production, green-Peak, blue-Decay, purple-Cylinder)

The rms-velocity profiles along the grid-element centreline are shown in figure 6a together with the experimental results of Laizet *et al.* (2015). Again, the comparison is good which further proves that the turbulent flow generated by the grid-element is indeed resolved properly. The production, peak and decay regions can be clearly identified in the rms-velocity profile. Turbulent intensity is defined as in previous studies (Wissink & Rodi 2011b; Venema *et al.* 2011; Wissink & Rodi 2011a), $Tu = \sqrt{\frac{1}{3}\frac{\langle u_i u_i \rangle}{U_\infty^2}} \times 100\%$. We chose to present rms velocity profiles instead of turbulent intensity profiles solely because the former can be compared against available experiments. Yet, the variation of Tu is similar to that of u_{rms} (see figure 21a). In the upstream of the cylinder, the u_{rms} profile (as well as the Tu profile) reaches a plateau at around the edge of the stagnation boundary layer, much like the mean velocity profile, as shown in figure 6b. The values of Tu at the edge of boundary layer (i.e. at $x_c/D = -1.5$) for each case are reported in table 1. It is important to note that the oncoming turbulent intensities for the production and decay cases are approximately similar, but the incident Reynolds numbers differ.

The profiles of mean velocity along the cross-stream direction y/D at different x_c/D locations upstream of the cylinder are plotted in figure 7. The x_c/D locations are chosen to be -5, -4, -3, -2, -1. At $x_c/D = -5$, although the profile of the cylinder case is uniform in the cross-stream direction, the profiles of other cases exhibit velocity deficits around $y/D \approx \pm 3$ due to the presence of grid-element bars. This velocity deficit is more prominent for the production and peak cases, while it is weaker for the decay case. This is expected as the production and peak regions are closer to the grid-element, while the decay region is further away. Downstream of $x_c/D = -5$, the wake deficits decrease in magnitude and the profile becomes more uniform. At $x_c/D = -2$, the velocity for the cylinder and decay cases almost match each other. The profiles at $x_c/D = -1$ clearly feel the presence of the cylinder. At the grid-element centreline, the value of mean velocity is the highest for the production case due to the jet-like behaviour discussed earlier. For the cases of cylinder and decay, the mean velocity at the grid-element centreline is observed to be similar, ascertaining the conclusions made earlier on the mean velocity evolution along the streamwise direction. Although the transverse average of the mean velocity profiles of the decay case is not 1, we noted the yz-plane-averaged velocity as 1. Therefore, mass conservation is indeed satisfied in all our simulations.

The development of u_{rms} profiles upstream of the cylinder is illustrated in figure 8. The presence of grid-element bars make the turbulence in the production and peak cases highly inhomogeneous with higher values behind the bars. On the other hand,
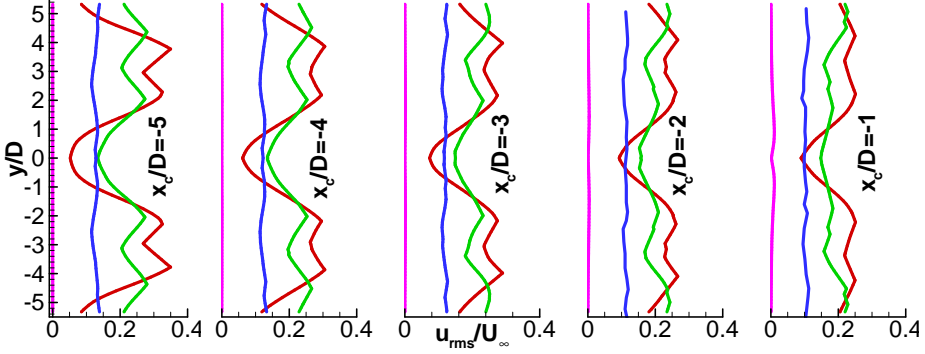
Figure 8: Development of rms velocity profiles upstream of the cylinder in the plane $z/D=0$ (red - Production, green-Peak, blue-Decay, purple-Cylinder)
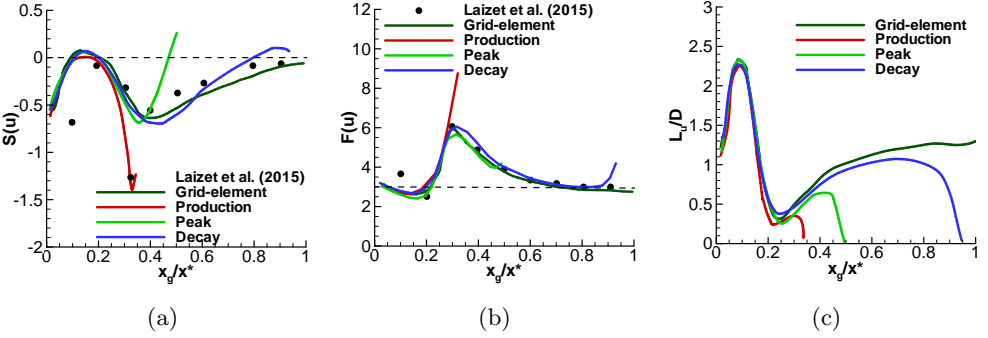

Figure 9: Variation of skewness, flatness and length scales of turbulence along the grid-element centreline: (a) Skewness, (b) Flatness, (c) Length scale.

the turbulence appears to be nearly homogeneous for the decay region. Mazellier & Vassilicos (2010) reported that the turbulence behind a fractal grid becomes approximately homogeneous around $x \approx x^*$. Therefore, it is not surprising that the turbulence upstream of the cylinder in the decay region is nearly homogeneous. The values of u_{rms} at $y/D = 0$ are similar for the production and decay regions at $x_c/D = -2$ and -1.

3.2. *Statistical characteristics of the oncoming turbulence*

The oncoming turbulence is further characterised using the skewness and flatness of the streamwise fluctuating velocity. Their profiles are depicted in figures 9a and 9b respectively. For Gaussian distribution, the skewness and flatness are 0 and 3 respectively; these are shown as dashed lines in figures 9a and 9b. Comparison with the experimental results of Laizet *et al.* (2015) is good, especially for flatness. In the production region, both skewness and flatness deviate from the Gaussian values. Large negative values of skewness in the production region represent extreme decelerating turbulent events (Mazellier & Vassilicos 2010), while the large positive values of flatness denote intense rare events. Therefore, the production region is identified as non-Gaussian with intense rare events of
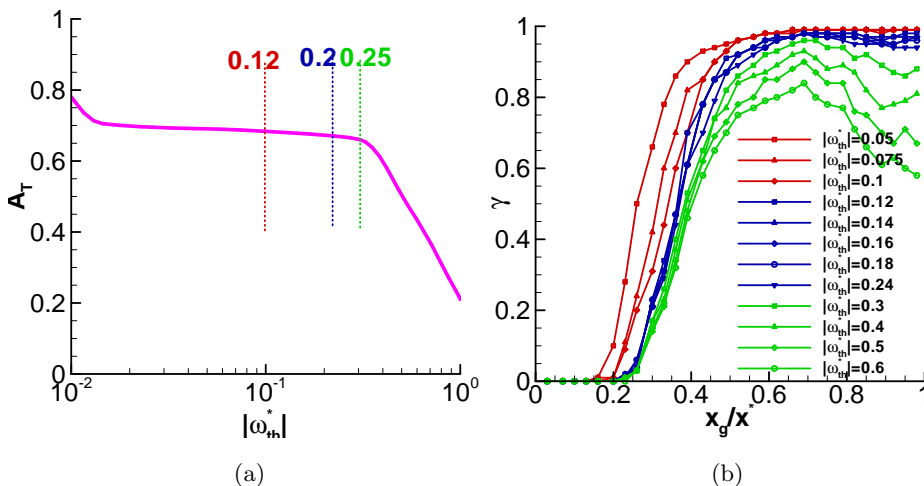
Figure 10: (a) Calculation of vorticity magnitude threshold, (b) Sensitivity of intermittency factor on vorticity magnitude threshold.

decelerating turbulence. In the decay region, the values of skewness and flatness indicate that the turbulence is closer to Gaussian. It is interesting to observe that placing a cylinder in the production region further decelerates the turbulence (figure 9a) and aids the creation of even more intense events (9b). However, such an observation is not made for the peak region and decay region cases.

The integral length scale (L_u) of the oncoming turbulence is computed using the time auto-correlation of fluctuating streamwise velocity defined as, $R_{uu}(\tau) = \langle u(t)u(t + \tau)\rangle/u_{rms}^2$. An integral time scale is computed as $L_{time} = \int_0^{R_\psi} R_{uu}(\tau)d\tau$, where R_ψ is the first zero crossing of $R_{uu}(\tau)$. This time scale is multiplied by the local mean velocity to obtain the integral length scale: $L_u = U_{local}L_{time}$. L_u normalised by the diameter of the cylinder is plotted in figure 9c. The integral length scale profile qualitatively resembles that of Valente & Vassilicos (2011) reported for a fractal grid.

3.3. *Characterisation of oncoming turbulence intermittency*

Finally, the intermittency of the oncoming turbulence is analysed. The study of intermittency is pertinent as the flatness of fluctuating streamwise velocity indicated that the production and peak regions are dominated by rare intense events. The intermittency factor (γ) is determined from the instantaneous magnitude of the vorticity vector $(|\boldsymbol{\omega}^*|)$, with components $\omega_i^* = \epsilon_{ijk}\frac{\partial u_k^*}{\partial x_j}$. Following studies on turbulent/non-turbulent interfaces (Bisset *et al.* 2002; Watanabe *et al.* 2014; Taveira *et al.* 2013; Zhou & Vassilicos 2017), the flow is defined as turbulent when $|\boldsymbol{\omega}^*|$ is greater than a certain threshold, $|\boldsymbol{\omega}^*|_{th}$. The intermittency factor is defined as, $\gamma =$ probability of $(|\boldsymbol{\omega}^*| \geqslant |\boldsymbol{\omega}^*|_{th})$. As can be seen from this definition, the vorticity threshold value plays a crucial role in determining the intermittency factor. The method adopted for estimating $|\boldsymbol{\omega}^*|_{th}$ in this study closely follows that of Taveira *et al.* (2013) and Zhou & Vassilicos (2017). Since this study focuses only on the grid-element centreline $z = 0$ plane, a two-dimensional instantaneous vorticity slice with dimensions $0 \leqslant x \leqslant 0.5x^*$ and $-5.3D \leqslant z \leqslant 5.3D$ is considered in this plane. A wide range of $|\boldsymbol{\omega}^*|_{th}$ values from 0 to 10 was considered. For each value of $|\boldsymbol{\omega}^*|_{th}$,
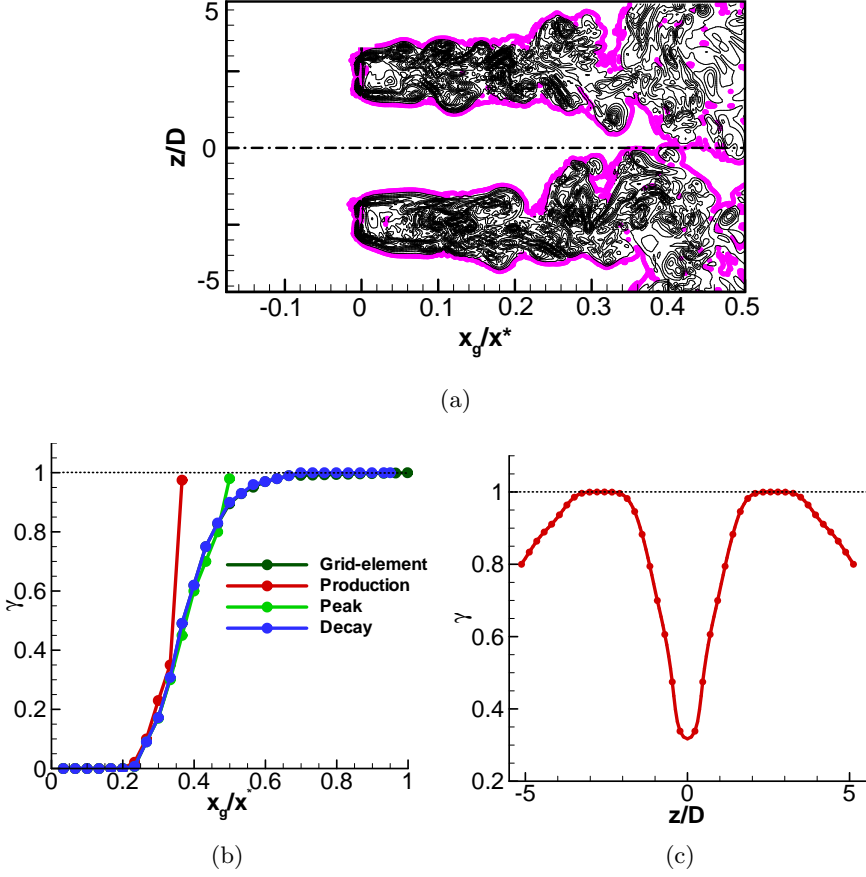
(a)

(b)

(c)

Figure 11: (a) Visualisation of the turbulent/non-turbulent (T/NT) interface and vortical structures surrounding the centreline. The 2D region plotted in this figure has the dimensions of $-5.3 \leqslant z/t_0 \leqslant 5.3$, and $0 \leqslant x_g/x^* \leqslant 0.5$ downstream of the grid-element. The purple lines represent the T/NT interfaces with $|\boldsymbol{\omega}^*|_{th}$=0.2 while the black lines represent the isolines of $0 \leqslant |\boldsymbol{\omega}^*| \leqslant 3$. (b) Evolution of intermittency factor along the grid-element centreline. (c) Evolution of intermittency factor along the spanwise direction at x_g/x^*=0.35 for the production case.

the fraction of turbulent area A_T = Area of$(|\boldsymbol{\omega}^*| > |\boldsymbol{\omega}^*|_{th})/max(A_T)$ is computed. The variation of A_T with $|\boldsymbol{\omega}^*|_{th}$ is depicted in figure 10a. A plateau can be seen for a range of $|\boldsymbol{\omega}^*|_{th}$ values. It is generally believed that the intermittency factor weakly depends on $|\boldsymbol{\omega}^*|_{th}$ when the threshold is chosen to be in this plateau (Watanabe *et al.* 2014; Taveira *et al.* 2013; Zhou & Vassilicos 2017). This is checked in figure 10b which shows the variation of intermittency factor for various $|\boldsymbol{\omega}^*|_{th}$. The profile of γ is found to be insensitive to $|\boldsymbol{\omega}^*|_{th}$ when $0.12 \leqslant |\boldsymbol{\omega}^*|_{th} \leqslant 0.25$. Therefore, we choose $|\boldsymbol{\omega}^*|_{th} = 0.2$.

The detected T/NT interface using this threshold value is visualised in figure 11a. The figure shows that the vortical structures are enveloped by the interface. The value of $|\boldsymbol{\omega}^*|_{th}$ depends on the flow configuration. For example, Bisset *et al.* (2002) reported a value of 0.7 for the far-wake of a cylinder, while for jet it is found to be 0.3 (Watanabe
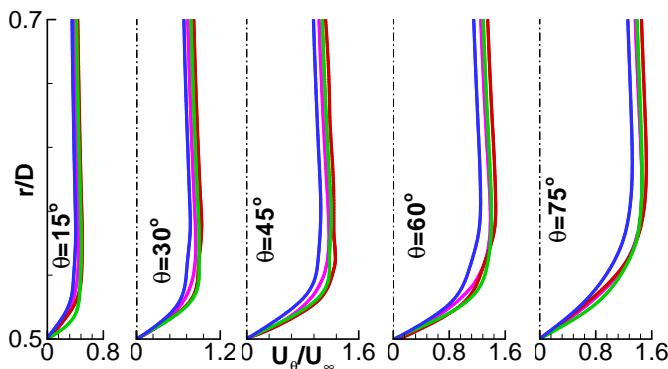
Figure 12: Mean azimuthal velocity profiles inside the boundary layer in the $z/D = 0$ plane (red - Production, green-Peak, blue-Decay, purple-Cylinder).

et al. 2014). The variation of intermittency factor along the grid-element centreline for all the cases is presented in figure 11b. As can be seen, the region $0 \leqslant x_g/x^* \leqslant 0.2$ is purely irrotational and the region $0.2 \leqslant x_g/x^* \leqslant 0.5$ is intermittent. Note the rapid increase of γ for the production and peak cases in points situated inside the developing boundary layer on the surface of the cylinder. This analysis reveals that the oncoming flow is indeed highly intermittent for the production case, less intermittent for the peak case and fully turbulent for the decay case. Since the cylinder is placed at $x_g/x^*=0.35$ for the production case, we also need to quantify the intermittency factor along the spanwise direction for this particular case. This information is provided in Figure 11c where one can note some intermittecy of the order of $\gamma=0.8$ in the region between $z/D = \pm 5.3$ and $z/D = \pm 4$. As a result, we choose $z/D = \pm 5$ for further analysis in the rest of the paper besides the grid-element centreline for the production case. Therefore, we have intermittent flow both at the grid-element centreline (i.e $z/D = 0$) and at $z/D = \pm 5$ of the production case.

As an interim summary, the oncoming turbulence generated by the single square grid-element has the following characteristics downstream of the grid-element: in the production and peak regions, the turbulence is highly non-Gaussian, inhomogeneous, and intermittent; on the other hand, at the decay region is Gaussian, approximately-homogeneous and fully turbulent.

4. Flow characteristics on the surface of the cylinder

Having examined the characteristics of oncoming turbulence, this section provides details on the flow characteristics around the surface of the cylinder.

4.1. *Mean velocity and turbulent stress profiles inside the boundary layer*

The azimuthal velocity profiles at different angles are compared in figure 12 for all cases considered. The variation in the radial direction, normal to the cylinder surface at plane $z/D = 0$, is plotted. The value of mean azimuthal velocity at the front stagnation, at $\theta = 0^o$, is zero due to symmetry. Moving clockwise, the velocity gradually increases. The boundary layer theory predicts that the thickness of the laminar boundary layer at the stagnation point (δ) has a power-law relationship with Reynolds number as, $\delta/D=Re_D^{-0.5}$
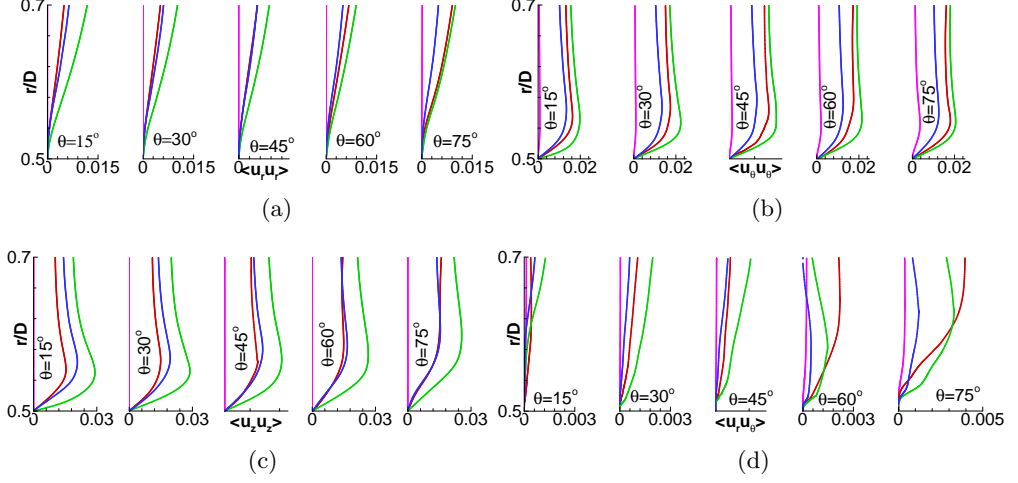
Figure 13: Hydrodynamic stress profiles inside the boundary layer in the $z/D = 0$ plane: (a) Radial stress, (b) Azimuthal stress, (c) Spanwise stress, (d) Reynolds stress. (red - Production, green-Peak, blue-Decay, purple-Cylinder).

(Zdravkovich 1997). This relationship appears to be satisfied for the cases considered in this study, as the simulations indicate a boundary layer thickness of $0.05D$ at $\theta = 0^o$, a value close to the theoretical prediction. Despite being exposed to turbulent fluctuations, the boundary layer profiles of production, peak and decay cases are comparable to the cylinder case. This indicates that the boundary layer on the surface of the cylinder in all cases could be laminar. Indeed, Jones & Launder (1973) showed that the boundary layer remains laminar for acceleration parameter K, defined as $K = \frac{\nu}{U_\infty^2} \frac{dU_\theta}{ds}$ (where ds is the circumferential distance on the surface of the cylinder) in excess of 2.5×10^{-6}. We measure U_θ at r/D=0.7. The value of K at 75° is computed to be around 3.5×10^{-6}, a value close to the critical value. Therefore, the boundary layer flow in the range of $0^o \leqslant \theta \leqslant 75^o$ is not fully laminar.

The turbulent stress profiles along the radial direction are plotted in figure 13. The stresses considered here are: (i) radial stress ($\langle u_r u_r \rangle$), (ii) azimuthal stress ($\langle u_\theta u_\theta \rangle$), (iii) spanwise stress ($\langle u_z u_z \rangle$) and (iv) Reynolds stress ($\langle u_r u_\theta \rangle$). They are all normalised by U_∞^2. The effect of free-stream turbulence has penetrated inside the boundary layer, as the stress magnitudes are larger near the cylinder surface for the production, peak and decay cases while they are zero for the cylinder case. Within the boundary layer, the azimuthal and spanwise stresses are higher than the radial stress, due to wall blocking that suppresses the latter. The magnitude of stresses gradually increases moving clockwise from the front stagnation point. The peak case exhibits the largest stress at all locations as the oncoming turbulence intensity is maximum. The radial and spanwise stress profiles collapse for the production and decay cases, especially for $\theta \geqslant 45^o$. This is not the case however for the azimuthal as well as the Reynolds stress profiles.

The effect of free-stream turbulence on the skin-friction coefficient (C_f) along the circumference of the cylinder is shown in figure 14. The mean separation angles, θ_s, for the cylinder, production, peak and the decay cases are computed to be 93.5, 100.2, 103.5, and 97 respectively. The higher values of separation angle for the production, peak and decay cases compared to that of the cylinder case signify the influence of free-stream
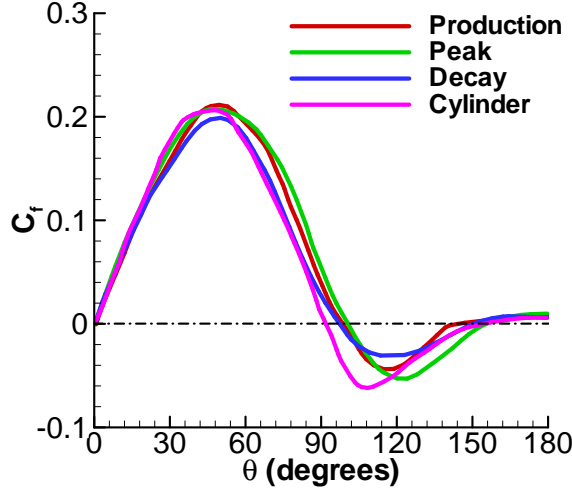
Figure 14: Variation of friction coefficient along the circumference of the cylinder in the $z/D = 0$ plane.
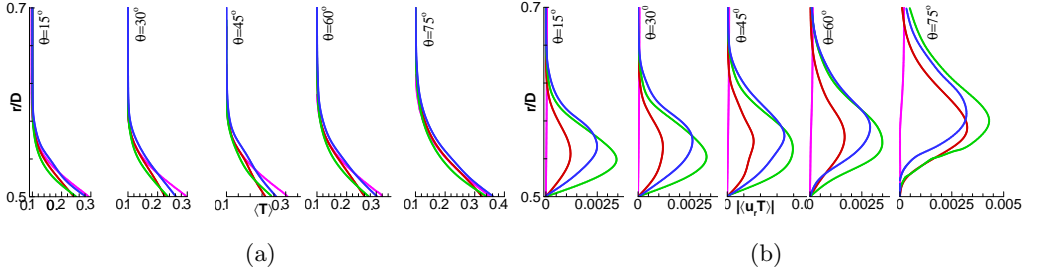

Figure 15: (a) Mean temperature profiles inside the thermal boundary layer in the plane z/D=0, (b) Wall-normal turbulent heat-flux ($|\langle u_r T \rangle|$) profiles inside the thermal boundary layer in the plane z/D=0 (red - Production, green-Peak, blue-Decay, purple-Cylinder).

turbulence in energising the laminar boundary layer and delaying its separation from the cylinder surface.

5. Heat transfer characteristics on the surface of the cylinder

This section explores the effect of free-stream turbulence on heat transfer characteristics.

5.1. *Mean temperature and turbulent heat-flux profiles inside the boundary layer*

Figure 15a shows the thermal boundary layer profiles at different angles. These profiles are normalised by $q_w D/k$, where k is the thermal conductivity. The thermal boundary layer is thicker than the hydrodynamic, because $Pr < 1$ and therefore the thermal diffusion is larger than the viscous diffusion. Indeed, the thickness δ_T is approximately 0.1D,
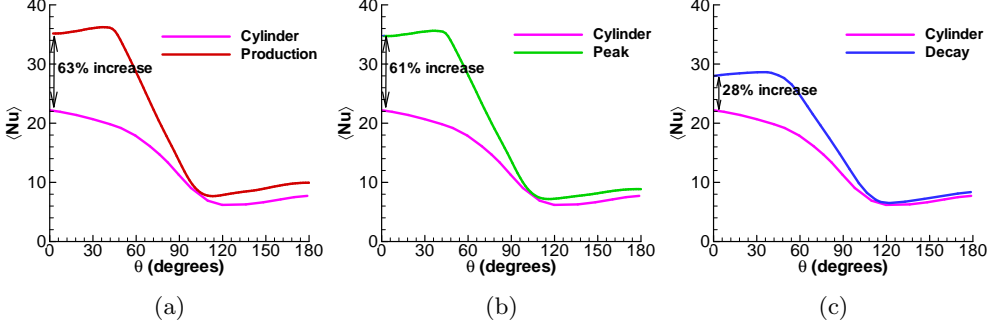
Figure 16: Variation of mean Nusselt number along the circumference of the cylinder in the plane $z/D=0$: (a) Production, (b) Peak, (c) Decay.

which is twice the hydrodynamic boundary layer thickness, δ. The mean temperature profiles of the production, peak and decay cases exhibit larger gradients compared to the cylinder case, indicating larger heat transfer. Between production and decay cases, the former has clearly larger gradients, and therefore higher heat transfer rate is expected. These observations are verified in the time averaged Nusselt number ($\langle Nu \rangle$) profiles, presented in the following subsection.

The wall-normal heat-flux profiles ($|\langle u_r T \rangle|$) are depicted in figure 15b. The presence of the cylinder blocks the radial fluctuation u_r, and therefore the heat transfer near the cylinder is mainly due to molecular diffusion (Wissink & Rodi 2011a). Moving clockwise from $\theta = 0^o$, the wall-normal region where turbulent fluctuations are active is expanding radially outwards from the surface. The maximum turbulent heat-flux is observed in the peak case, as expected. Comparing the profiles of the production and decay cases, the decay case has larger turbulent heat-flux than the production case.

5.2. *Effect of free-stream turbulence on Nusselt number profiles*

The variation of mean Nusselt number, $\langle Nu \rangle$, for the production, peak, and decay cases is shown in figures 16a, 16b and 16c respectively. The $\langle Nu \rangle$ for the cylinder case is also plotted for comparison. The observations noted from the mean temperature and turbulent heat-flux profiles are reflected in the $\langle Nu \rangle$. The heat transfer rate of the production, peak and decay cases are higher than that of the cylinder. The maximum increase of heat transfer at the front stagnation point occurs for the production case with a substantial 63% rise. On the other hand, the peak case, which has a maximum oncoming turbulence intensity of 15%, results in 61% increase. The decay case exhibits the smallest increase of 28%, although the oncoming turbulent intensities of the production and decay cases are similar.

It can be argued that the increase of the incident velocity for the production and peak cases can explain the observed heat transfer enhancement. Therefore, we need to account for the effect of different Reynolds numbers on the stagnation point Nusselt number, $\langle Nu_0 \rangle$. Table 2 compares the present $\langle Nu_0 \rangle$ against the values predicted by theory using the correlation $\langle Nu_0 \rangle = 0.95 Re_D^{0.5}$ (Krall & Eckert 1973). The cylinder case value of $\langle Nu_0 \rangle$ is closer to the one obtained by Krall & Eckert (1973). The results also reveal that the effect of the present Reynolds number range is weak when there is no oncoming turbulence and, therefore, cannot explain the large increase predicted in the

Simulation name	Re_{inc}	$\langle Nu_0 \rangle$ (theory)	$\langle Nu_0 \rangle$ (present)	% increase
Cylinder	500	21.24	21.90	1.60%
Production	600	24.49	35.12	44%
Peak	550	23.45	34.9	49%
Decay	500	22.0	28.1	28%

Table 2: Effect of incident Reynolds number on stagnation point heat transfer coefficient.

production region. The largest deviation from theory is observed for the peak case, and the smallest for the decay case. This observation is expected as the peak case has the highest oncoming turbulent intensity of all other cases. It is interesting, however, to note that the production case has much higher heat transfer increase than that of the decay case although both cases have a similar turbulent intensity value. Clearly, the difference in heat transfer enhancement is not due to differences in the incident Reynolds number. The reasons are explored later in this study by means of timescale separation analysis and examining the dominant frequency of the turbulent fluctuations.

The next important observation in the $\langle Nu \rangle$ profiles (figures 16) is the location of the maximum. The front stagnation point on the surface of the cylinder is expected to have the highest heat transfer rate. This is because the cold oncoming flow makes contact with the cylinder surface first on the front stagnation point. As the flow warms up, the rest of the cylinder surface is exposed to flow with higher temperature than the one that has impinged on the front stagnation point (Paul *et al.* 2016). This observation is valid only in the cylinder case, when there is no oncoming turbulence. When a turbulence-generating grid-element is introduced, figures 16a-16c show that the $\langle Nu \rangle_{max}$ is shifted around 45° away from the front stagnation point. Similar observations have been noted in the experimental study of Magari & LaGraff (1994) and the semi-DNS study of Venema *et al.* (2011). In those studies the cylinder was subject to wake turbulence generated by a small cylinder placed upstream. They concluded that the shift in $\langle Nu \rangle_{max}$ is due to the presence of the small cylinder which creates a wake deficit which in turn decreases the convective heat transfer at the front stagnation point. The study of Wissink & Rodi (2011*a,b*), where the wake generator was simulated in a precursor simulation and the turbulence data was imposed on the inlet of the domain, could not detect such a shift in $\langle Nu \rangle_{max}$.

In order to gain more insight on the effect of flow on heat transfer, contour plots of $\langle Nu \rangle$ on the surface of the cylinder are shown for all the cases in figure 17. For the cylinder case, the $\langle Nu \rangle$ contour is uniform in the spanwise direction (figure 17a) as expected. The presence of the vertical bars of the grid-element results in non-uniform distribution of $\langle Nu \rangle$ in the spanwise direction. This is attributed to the fact the local velocity, turbulent intensity and integral length scales vary drastically along the spanwise direction. As can be seen in figure 17b, $\langle Nu \rangle$ attains its maximum value around $\theta \approx 45^o$ along the grid-element centreline. This feature is more prominent in the production case and becomes milder for the decay case. Since the grid-element centreline is not directly immersed in the wakes of the bars, there is no wake deficit, and so the argument of Venema *et al.* (2011) cannot explain why the location of $\langle Nu \rangle_{max}$ is shifted from the front stagnation point. We propose a novel explanation for this observation in the next subsection.
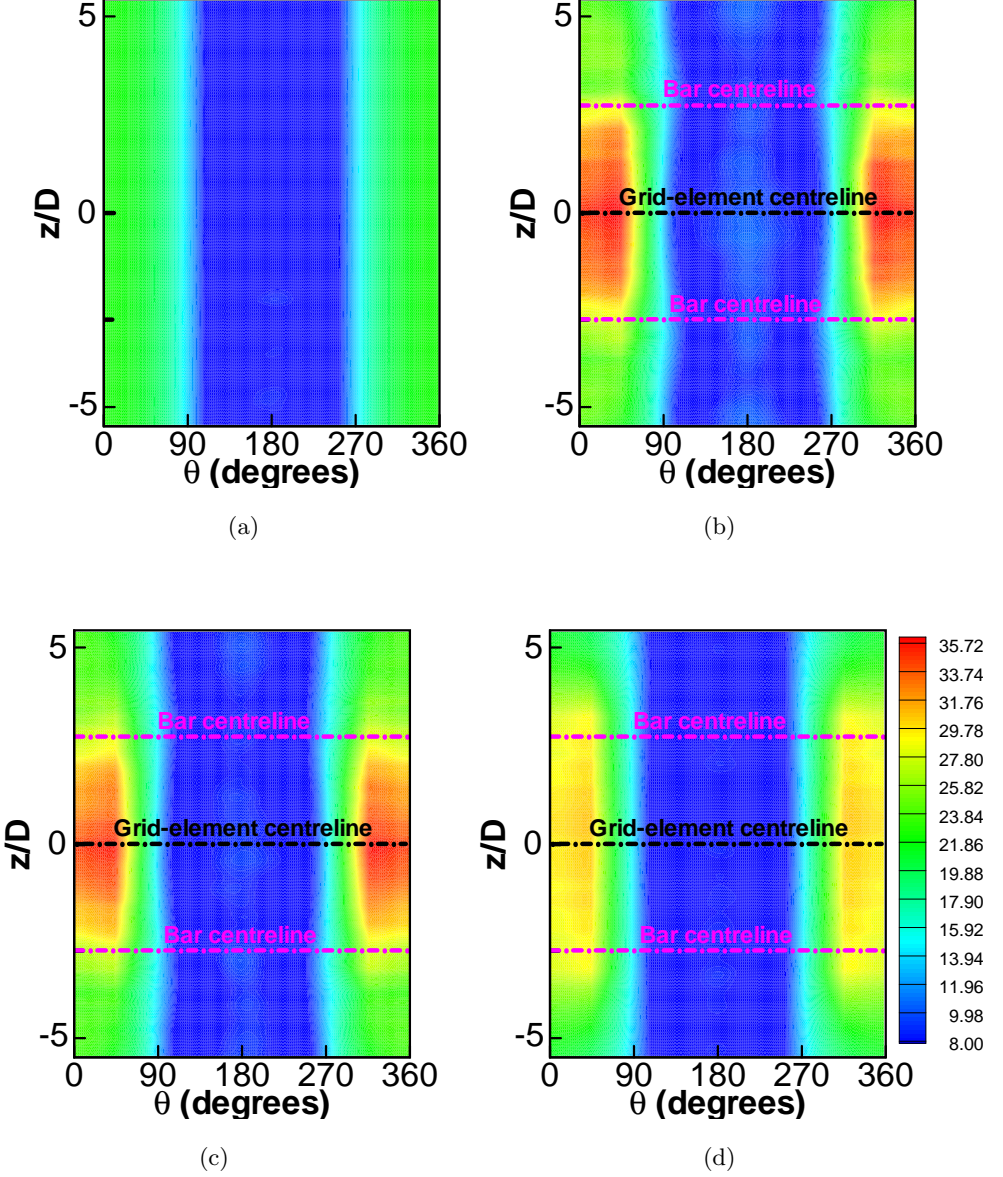
Figure 17: Contours of mean Nusselt number on the cylinder surface: (a) cylinder, (b) Production, (c) Peak, (d) Decay. The isocontours range from 8 to 36.

Figure 17b also reveals yet another intriguing behaviour. We know that the oncoming flow characteristics at the grid-element centreline (i.e. $z/D = 0$) and at $z/D = \pm 5$ of the production case are similar, meaning that both are intermittent, non-Gaussian and inhomogeneous. The only difference between these two locations (i.e. $z/D = 0$ and $z/D = \pm 5$) is the turbulent intensity values. At $z/D = 0$, the oncoming turbulent intensity is 11% while it is roughly 24% at $z/D = \pm 5$. On the other hand, $\langle Nu \rangle_0 \approx 35.3$ at $z/D = 0$

while it is only 25.1 at $z/D \pm 5$. These values and figure 17b vividly reveal that neither the intermittent, non-Gaussian nature of the flow nor the turbulent intensity are the most important parameters for the heat transfer. Note also that although the turbulent intensity is very high along the bar-centreline, in particular for the production case (see figure 21a), the maximum $\langle Nu \rangle$ is not observed along the bar centreline, instead it is located at the grid-element centreline. These observations also testify that the flow along the grid-element centreline has some unique characteristics that cause higher heat transfer for a lower oncoming turbulent intensity. These unique characteristics are explored in §7 and §8.

Finally, we can note that the $\langle Nu \rangle$ contour of the decay case, shown in figure 17d, is non-uniform along the spanwise direction although the oncoming turbulence is similar to the one considered in the literature. It appears that the flow at the decay region is only approximately homogeneous and it still remembers the upstream condition. Due to this reason, non-uniformity in $\langle Nu \rangle$ is not fully vanished for the decay case. Note also that the experiments, that used regular grids to generate oncoming turbulence, placed cylinders after $x/x^* \approx 4$ from the grid. Therefore, their results cannot be compared with our result in figure 17d as we are still in the near-field of the grid and the flow is not fully disconnected from the upstream conditions.

5.3. *Factors causing the shift in the location of $\langle Nu \rangle_{max}$*

The shift in the location of $\langle Nu \rangle_{max}$ from the front stagnation point is further explored through probability density functions (PDFs) of Nusselt number at various azimuthal locations, plotted in figure 18. The PDFs of Nusselt number for the cylinder case appear to be Gaussian with a near-perfect symmetry. The other cases exhibit an interesting behaviour. The PDF at the stagnation point appears to be near-symmetric with a Gaussian profile. Yet, for the region of $0^o < \theta \leqslant 45^o$, the PDFs lose their symmetry with more skewness towards higher values of Nu. The level of skewness increases from $\theta > 0^o$ to $\theta \approx 45^o$. After $\theta \approx 45^o$, the PDFs again translate to a near-symmetric shape for the production, peak and decay cases. It appears that additional intense events occur in the region of $0 < \theta \leqslant 45$ compared to the front stagnation point that cause the skewness of the PDFs. Such events can be more clearly seen in figure 19 where the PDFs of Nusselt number at the front-stagnation point and at $\theta = 45^o$ are compared. The green shaded areas in these figures represent the additional intense events occurring at $\theta = 45^o$. Note that the shaded area in these figure is largest for the production case, and progressively decreases in the peak and decay cases. These events cause the PDFs of Nusselt number to skew more towards higher values, resulting in higher heat transfer rate at $\theta = 45^o$.

Having identified the presence of intense events at $\theta = 45^o$, the question now is what causes such events. The answer can be found in the oncoming turbulence profiles. It is known that the Nusselt number is primarily a function of Reynolds number, turbulent intensity, and length scales. The length scales are not expected to change drastically in the limited range of $0 \leqslant \theta < 45^o$. However, the profiles of mean velocity show that there exists a jet-like behaviour as discussed earlier. Therefore, the cylinder sees a much higher velocity at locations $0 < \theta \leqslant 45$ as seen in figure 7 for x_c/D=-1. Adding to that, the oncoming turbulence intensity is also highly inhomogeneous in the cross-stream direction with lesser intensity at the stagnation point and higher values away from it (see figure 8). Therefore, it is believed that the increase in local mean incident flow and its turbulent intensity at $\theta \approx 45^o$ compared to the front stagnation point is related to the additional intense events which in turn shift the $\langle Nu \rangle_{max}$ by 45° from the stagnation point.
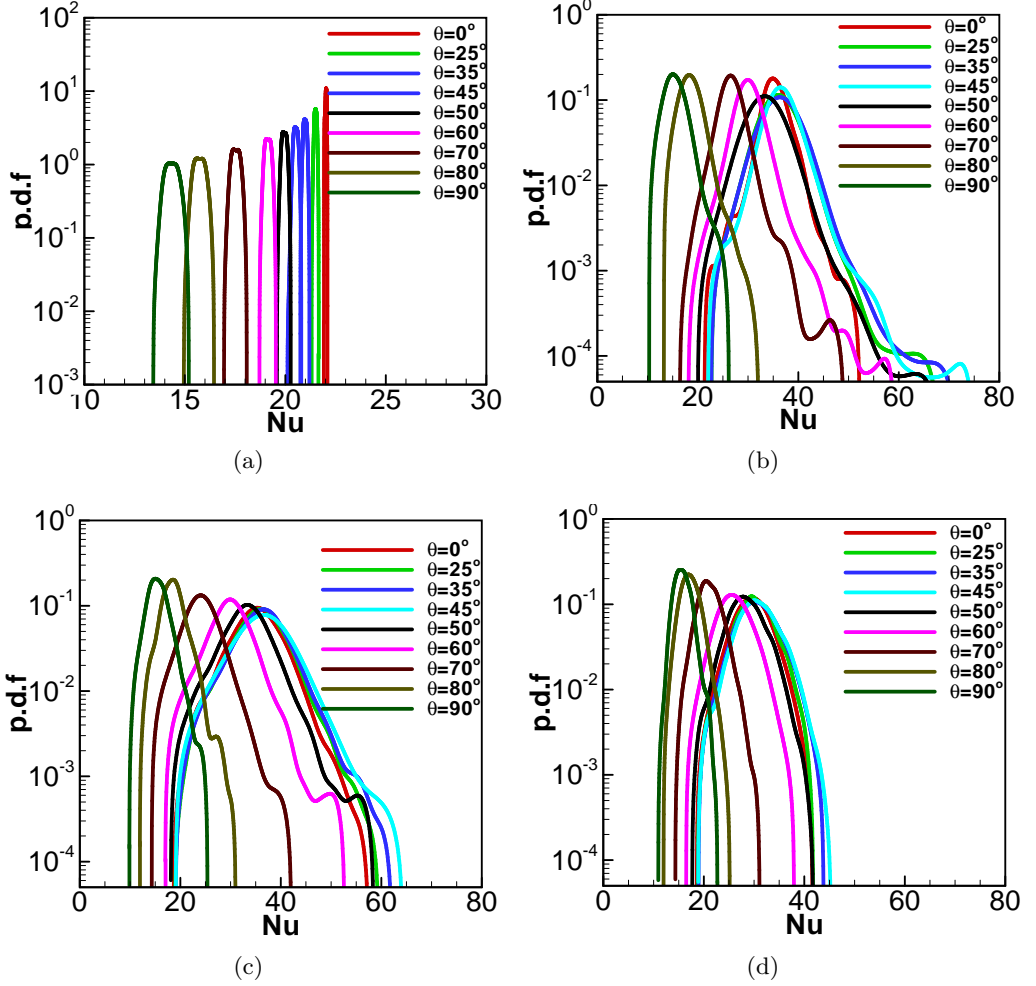
Figure 18: PDFs of Nusselt number at different locations along the circumference of the cylinder in the plane z/D=0: (a) Cylinder, (b) production, (c) peak, (d) decay

6. Validity of the existing stagnation-point heat transfer correlations

The validity of existing correlations for the stagnation point heat transfer coefficient is assessed in this section. These correlations are given by equations (1.1) and (1.2) and they require the calculation of free-stream straining, a_1. The value of a_1 is difficult to measure experimentally, and most of the experimental studies assume $a_1 = 4$ which corresponds to potential flow. The procedure outlined in Venema *et al.* (2011) is followed in this study to determine the value of a_1. On the grid-element centreline, a_1 is defined as $a_1 = -\frac{\partial U}{\partial x}\frac{D}{U_{inc}}$. The variation of a_1 along the centreline reaches a plateau around $x_c/D = -1.5$ (much like the plateau observed for mean and rms velocity profiles), and the values chosen from this plateau are 1.8, 2.8, 3.6, and 3.8 for the production, peak, decay, and circular cases respectively. The values of Nu_a and Tu_a are checked against the correlation curve in figure 20a. As the computation of a_1 involves uncertainties, the correlation parameters are also computed using the potential flow constant $a_1 = 4$. The closed symbols represent the computed values of a_1, while the open symbols represent
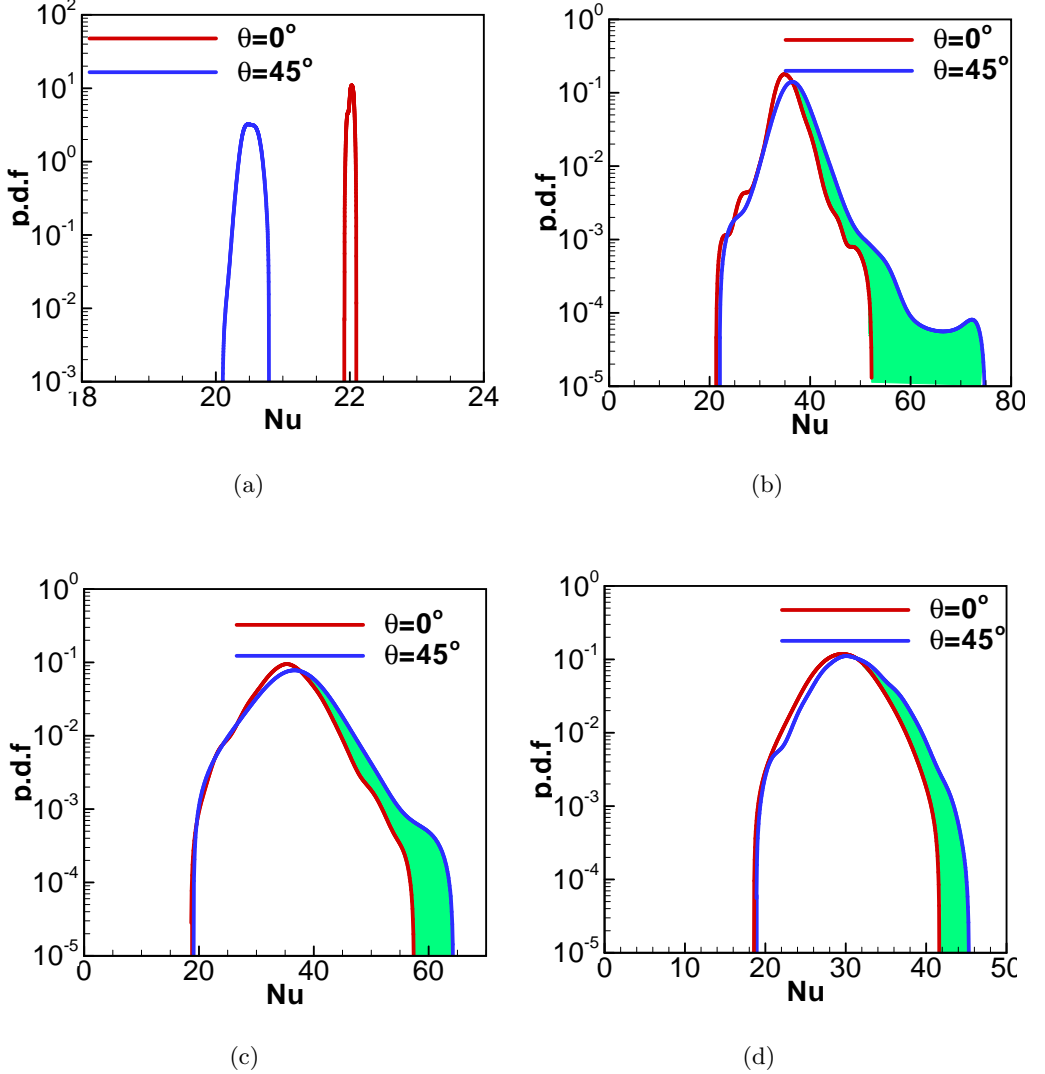
Figure 19: Illustration of additional intense events occurring at the $\langle Nu \rangle_{max}$ point in the plane $z/D{=}0$ for the case of: (a) Circular, (b) Production, (c) Peak, (d) Decay

the potential flow value. The cylinder case, which also forms the origin of the correlation curve, is well predicted. It is interesting, however, to note that the correlation curve is not valid for the production and peak cases, where the computed values are much higher, and outside the correlation error bound region. On the other hand, the correlation curve is satisfied in the decay case. One could presume that the exclusion of the turbulence length scale in equation (1.1) could be the reason why the correlation is not satisfied in the production and peak cases. Therefore, the correlation proposed by Dullenkopf & Mayle (1995), which includes the effect of the integral length scale (refer to equation (1.2)), is also assessed.

The two sides of the correlation equation (1.2) are computed and compared against the
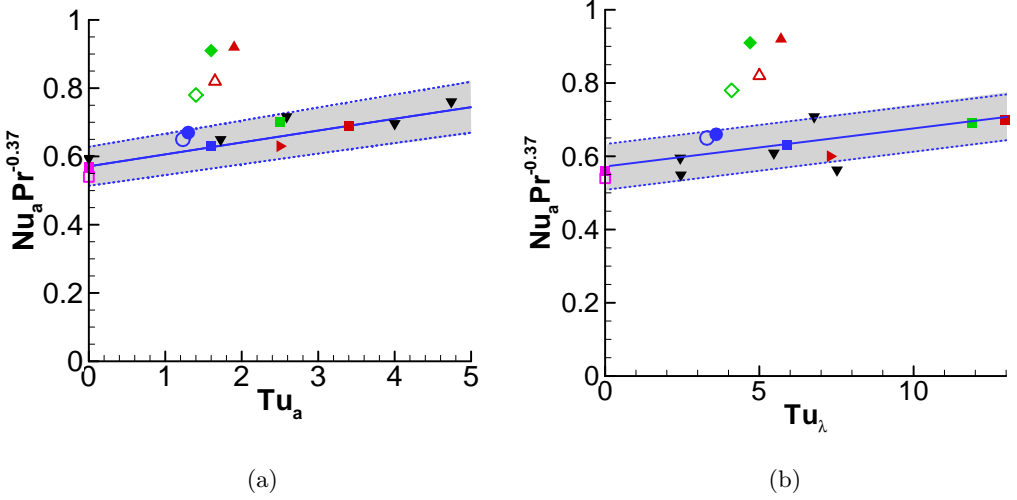
(a)   (b)

Figure 20: Assessment of (a) the correlation (1.1) of Dullenkopf & Mayle (1994) and (b) the correlation (1.2) of Dullenkopf & Mayle (1995). The square symbols represent data for the bar centreline (see figure 1c), and they are differentiated in terms of their colour as red - Production, green-Peak, blue-Decay, purple-Cylinder. The red-coloured right triangles are for the production case at $z/D=\pm5$. The filled inverted triangles are the literature data from Wissink & Rodi (2011a), Wissink & Rodi (2011b), Venema *et al.* (2011) and Venema *et al.* (2014). The other symbols represent the grid-element centreline correlations, and they are identified as, Triangle- Production, Diamond- Peak, Circle- Decay. The open symbols are the results obtained with the potential value of free-stream straining $a_1 = 4$, and the filled symbols are from the computed value of a_1. The dotted lines represent the $\pm5\%$ error bounds of the correlations.

correlation curve in figure 20b. It is observed that this correlation is also invalid for the production and peak cases, similar to the previous correlation. Therefore, the inclusion of length scale does not change the scenario. Note, however, that the parameter Tu_λ in (1.2) is for a spectra without any shedding frequency while the production and peak cases clearly have shedding effect (see figures 21b and 21b). Therefore, the correlation equation (1.2) is not fully reliable for the production and peak cases. Yet, it is intriguing to note that the production case at $z/D = \pm5$ does satisfy the correlations (1.1) and (1.2), where the flow is inhomogeneous, non-Gaussian and intermittent (look for right triangles in figure 20). The failure of both the existing correlations for the grid-element centreline indicates that the turbulence in the grid-element centreline production and peak cases possess some unique characteristics which produce higher heat transfer compared to previous studies. The reasons for this excessive heat transfer rate are discussed in the next two sections. Note also that this is the first DNS study that reports some invalidity of correlations (1.1) and (1.2). The previous numerical studies (Venema *et al.* 2011; Wissink & Rodi 2011a,b) showed that the correlation curves are valid for the case of wake turbulence generated by a small cylinder placed upstream of a larger cylinder. In the present configuration, the correlations are found to be valid also along the bar-centreline (see figures 20a and 20b for filled square symbols). It is indeed intriguing

to note that the presence of turbulence along the grid-element centreline exhibits such unusual heat transfer results, while the bar-centreline and the location $z/D = \pm 5$ exhibit results which are consistent with literature. This is the main reason, as mentioned at the beginning of this section, why this study focuses only on the $x - y$ plane which has the grid-element centreline (i.e. $z = 0$ plane).

7. Effect of the dominant frequency of fluctuations on heat transfer

This section initiates the investigation why the stagnation point heat transfer correlations are not valid in the production and peak cases. Receptivity theory states that the laminar boundary layer is sensitive (or receptive) to the free-stream disturbances only in a selective band of frequencies. The representative frequency of this band is obtained using receptivity theory as $f_\lambda = \lambda U_\infty / \delta$, where λ is a constant which was computed to be in the range of 0.01 to 0.04 (Schlichting & Gersten 2016). Therefore, it is not the root mean square of the fluctuations, but it is the spectral energy content of the fluctuations that determines the response of the boundary layer to the free-stream turbulence. For stagnation flows, the boundary layer thickness is $\delta \approx 2.4\sqrt{\nu/a}$ (Schlichting & Gersten 2016). Using this expression, Dullenkopf & Mayle (1995) derived an equivalent frequency to which the stagnation point boundary layer is most receptive and it is given as $f_\lambda = 0.03 U_\infty / \delta$. Using this expression, the normalised dominant frequency of fluctuations to which the stagnation boundary layer is most receptive, can be computed as

$$\phi_\lambda = \frac{f_\lambda D}{U_{inc}} 0.0125 \sqrt{Re_{inc} a_1} \qquad (7.1)$$

In order to investigate the effect of dominant frequency of fluctuations, the variation of turbulent intensity and its spectra at three locations along the bar and grid-element centrelines are presented in figure 21. The dominant frequency ϕ_λ is plotted in figures 21b, 21c and 21d along with the spectra of velocity fluctuations computed at a distance $1.5D$ upstream of the cylinder for both grid-element and bar centrelines. A selective bandwidth of frequencies ($\Delta\phi$) to which the boundary layer is receptive is also shown indicatively in the figure. This frequency band is constructed with the constraint $\Delta\phi/\phi_\lambda << 1$ as proposed by Dullenkopf & Mayle (1995). In this study, the ratio $\Delta\phi/\phi_\lambda$ is taken as 10^{-3}.

The turbulent intensity is very high in the near-field of the bar centreline, while both grid-element and bar centrelines have similar values of turbulent intensity far downstream (see figure 21a). At $x/x^* \approx 0.35$ (i.e. in the production region), although the turbulent intensity of the bar centreline is at least twice of the grid-element centreline (figure 21a), it is clear from figure 17b that the maximum heat transfer occurs only along the grid-element centreline. As seen in figure 21b, the dominant frequency range lies very close to the shedding frequency which has the highest energy content for the production case grid-element centreline while it lies in higher frequencies that have lower energy for the production case bar centreline. This means that although the rms of velocity fluctuations is higher for the bar centreline production case, their energy content at the dominant frequency is much lesser than that of the grid-element centreline. Therefore, they are not as effective as the grid-element centreline disturbances in penetrating the boundary layer.

The energy spectra and its dominant frequency range for the production case spanwise location $z/D = \pm 5$ is also plotted in black-coloured lines in figure 21b. Recall that the flow at this location shares similar characteristics to that of the flow along the production case grid-element centreline. That is, the flow is intermittent, non-Gaussian and inhomogeneous. At this location, oncoming turbulent intensity is 24%. Yet, the
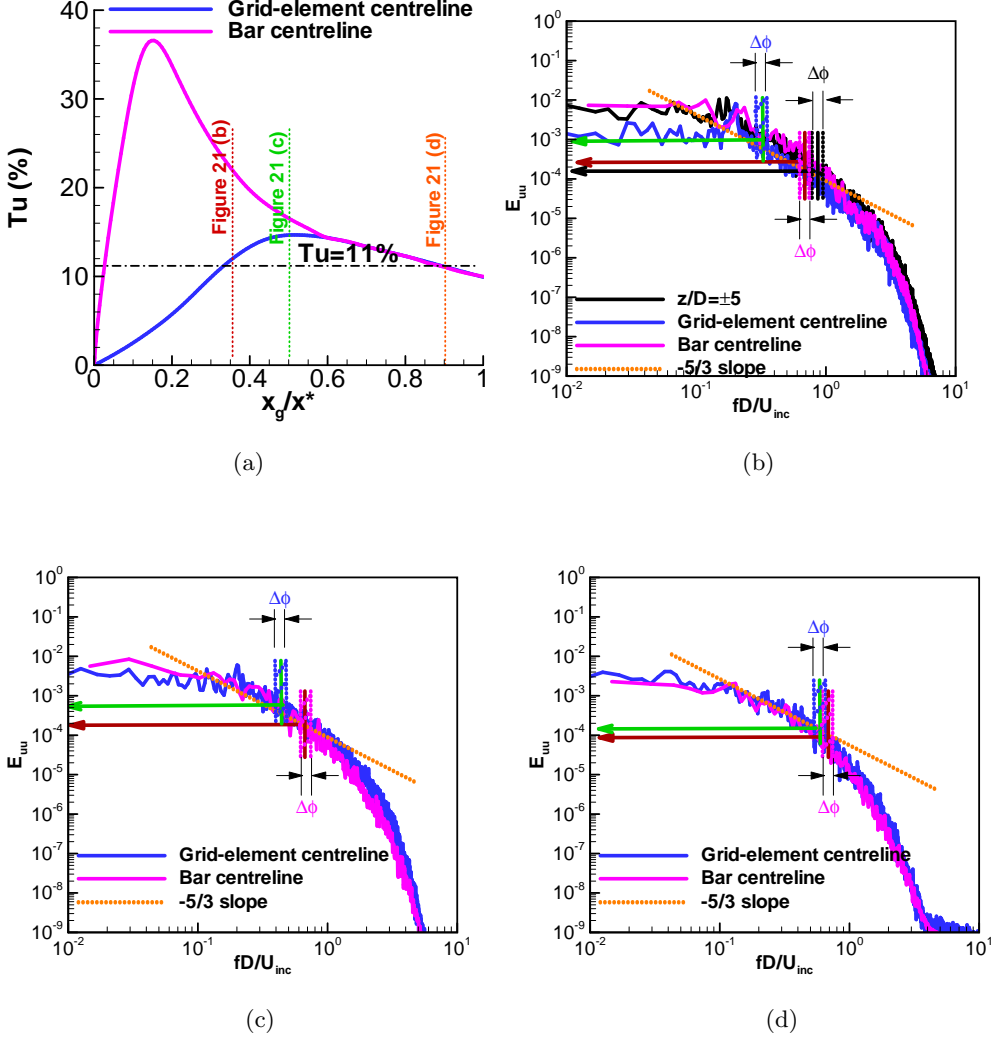
(a)

(b)

(c)

(d)

Figure 21: (a) Evolution of turbulent intensity along the bar and grid-element centrelines. (b,c,d) Energy Spectrum at x_c/D=-1.5 in the plane z/D=0: (b) Production, (c) peak, (d) decay. The dominant frequency and its corresponding spectral density in the grid-element and bar centrelines are marked by green and brown lines respectively. The dominant frequency range is indicatively marked with dotted blue and purple lines for the grid-element and bar centreline respectively. The spectra and its dominant frequency in black-coloured lines in (b) represent the production case at $z/D=\pm5$.

dominant frequency lies in higher frequencies as the mean straining behaviour here is equivalent to that of the bar-centreline. As a result, although the flow at $z/D = \pm5$ intermittent and has higher oncoming turbulent intensity, it is not as effective as the grid-element centreline flow to interact with the laminar boundary layer and thus to cause higher heat transfer.

One can note by comparing figures 21b and 21d that, along the grid-element centreline,
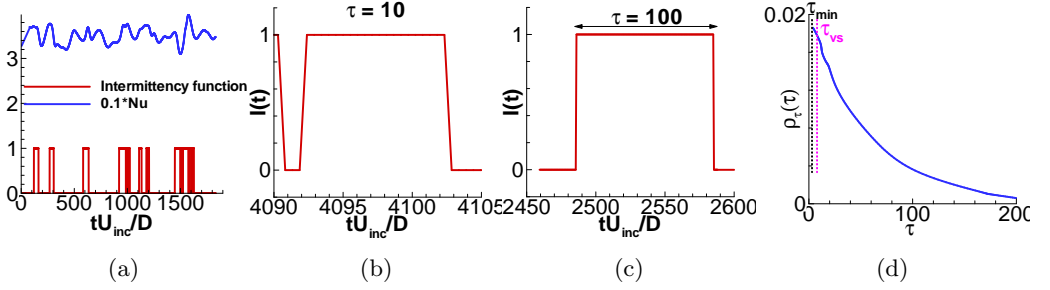
Figure 22: (a) A typical segment of intermittency function signal with the corresponding instantaneous Nusselt number. The Nusselt number signal is recorded at $x_c/D = -0.5$ (i.e. at the surface of the cylinder) while the intermittency function signal at $x_c/D = -1.5$, (b) An example of a shedding event, (c) An example of a non-shedding event, (d) Probability of timescales of turbulent events.

the energy content of the dominant frequency is higher for the production case while it is lower for the decay case, although the turbulent intensities are similar at 11% (see figure 21a). The higher energy content of the production region dominant frequency is one of the reasons why the grid-element production case results in very high heat transfer and thus fails to satisfy the existing stagnation point correlations. This evidence proves that the most important parameter for heat transfer increase is the dominant frequency of fluctuations rather than the turbulent intensity. In the next section, we further investigate the unusual heat transfer increase for the grid-element centreline production and peak cases.

8. Timescale separation analysis and mechanisms of heat transfer enhancement

In this section, a novel approach is used to provide more insight about the nature of the flow that causes higher heat transfer rate for the production case. A timescale analysis is performed at x_c/D=-1.5 (i.e at the edge of the laminar boundary layer where the plots of 21b, 21c and 21d were computed) as explained below. The turbulent flow events are identified at that point through the intermittency function, $I(t)$, which is defined as

$$I(t) = \begin{cases} 0, & \text{if } |\boldsymbol{\omega}^*(t)| < |\boldsymbol{\omega}^*{}_{th}| \\ 1, & \text{otherwise} \end{cases} \qquad (8.1)$$

where $I(t)$=0 means that the flow can be considered irrotational while $I(t)$=1 means it is turbulent. We choose $|\boldsymbol{\omega}^*{}_{th}|$=0.2 as determined in section 3.3. A typical intermittency function and the corresponding instantaneous Nusselt number signal is shown in figure 22a for the production case. Note that, while the intermittency function is computed at $x_c/D = -1.5$, the Nu signal is at the front stagnation point ($x_c/D = -0.5$). Therefore, the time-lag between these two points is approximately estimated from the distance between the points and the local mean velocity (U_{inc}). Consequently, the Nu signal is shifted in time according to the time-delay. As can be seen in figure 22a, the flow is highly intermittent, and the turbulent flow (i.e. the events for which I(t)=1) has a wide range of timescale events ($\tau = \Delta t U_{inc}/D$, where Δt is the time step of the turbulent event) ranging from short to long. Typical short and long timescale events are shown in figures
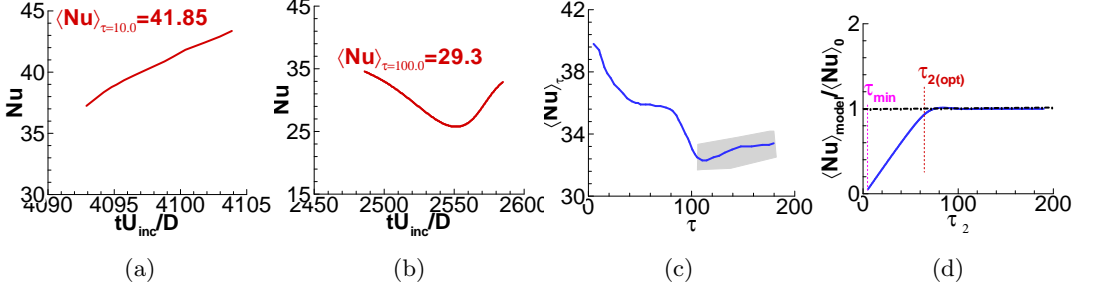
Figure 23: (a) Variation of instantaneous Nusselt number in a shedding event, (b) Variation of instantaneous Nusselt number in a non-shedding event, (c) Variation of conditional mean Nusselt number with respect to the time-scales of turbulent events, (d) Calculation of optimum τ_2.

22b and 22c respectively. Computing the probability of the timescale events ($\rho_\tau(\tau)$) for the entire signal reveals that the flow is dominated by shorter rather than longer timescale events (figure 22d). The smallest timescale event observed in our data set is represented as τ_{min}. As the current simulation has run for sufficiently long time (as evidenced by the well-converged statistics presented earlier), it is expected that the turbulent events of timescale $\tau < \tau_{min}$ could occur very rarely. The timescale of the short events, as noted in figure 22d, is comparable to the timescale of vortex shedding ($\tau_{vs} = 1/St$), where St is the Strouhal number ($St = f_{vs}D/U_{inc}$, see figures 21b-21d). Therefore, the short timescale events are called shedding events, while the long timescale events are called non-shedding events. In this way, the energetic shedding events that have a timescale of τ_{vs} are considered as equivalent to those with the dominant frequency (ϕ_λ). It must be stressed here that the Strouhal frequency in figure 21 is the frequency of the flow itself, while the frequency in figure 22d is only the representative frequency of a turbulent event.

Typical variations of instantaneous Nu for the shedding and non-shedding events are depicted in figures 23a and 23b respectively. The time averaged Nusselt number conditioned for every timescale event τ, $\langle Nu \rangle_\tau$, is given in figure 23c. The shaded area in this figure represents the lack of statistical convergence in $\langle Nu \rangle_\tau$ as only a few non-shedding events occur in the production case. Yet, the main interpretation from this figure is that the largest heat transfer occurs at the shedding events, and the value of $\langle Nu \rangle_\tau$ decreases for increasing τ. This signifies the importance of shedding events for higher heat transfer rates. These shedding events, as noted earlier, are able to penetrate the boundary layer, because they have a frequency close to ϕ_λ. The Nu values corresponding to $I(t) = 0$ events are found to be small compared with the events of $I(t)=1$.

Based on the DNS results of this study, a simple model for the mean Nusselt number is proposed. It is given as,

$$\langle Nu \rangle_{model} = \int_{\tau_{min}}^{\tau_2} \rho_\tau(\tau)\langle Nu \rangle_\tau d\tau \qquad (8.2)$$

Mathematically, equation (8.2) should be integrated from 0 to infinity. For intermittent flows, however, it is integrated from τ_{min} to τ_2. The optimum value of τ_2, $\tau_{2(opt)}$, is determined by integrating equation (8.2) for various values of τ_2 and $\tau_{2(opt)}$ is chosen to be the value of τ_2 for which the $\langle Nu \rangle_{model}$ becomes equal to the value computed by the simulations (see figure 23d). We observe that the optimum timescale event ($\tau_{2(opt)}$)
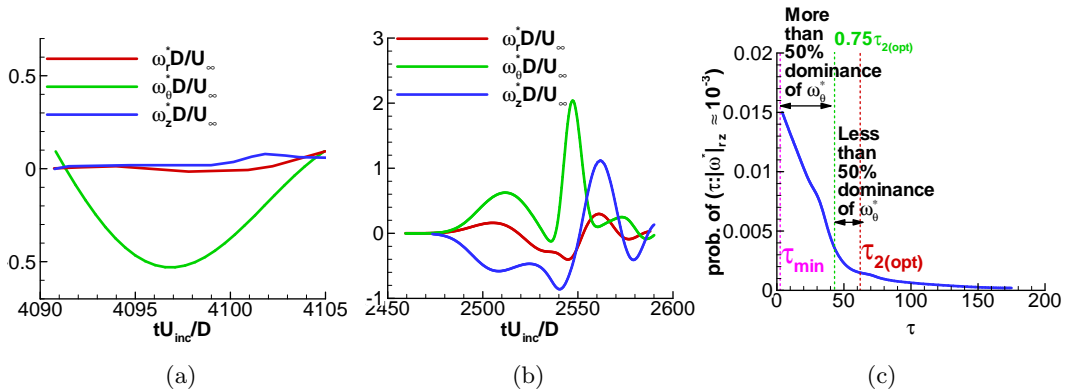
Figure 24: (a) Variation of vorticity components in a shedding event, (b) Variation of vorticity components in a non-shedding event, (c) Conditional probability of $|\boldsymbol{\omega}^*|_{rz} \approx 10^{-3}$.

is approximately six times of the shortest timescale event (τ_{min}). The timescale range $\tau_{min} < \tau < \tau_{2(opt)}$ is termed the effective timescale range for heat transfer. Note also that equation (8.2) is applicable only for production and peak cases as there is no proper way to compute $|\boldsymbol{\omega}^*_{th}|$ for the fully turbulent decay region.

Having identified the effective timescale range, the next step is to classify the shedding and non-shedding events based on this effective timescale range. To this end, the timescale events are further analysed using the instantaneous vorticity components decomposed with respect to the polar coordinates (similar to the velocity field). The radial, azimuthal, and spanwise components of instantaneous vorticity are denoted as ω_r^*, ω_θ^*, and ω_z^* respectively. Variations of vorticity components in the shedding and non-shedding events are shown in figures 24a and 24b respectively. It is interesting to observe that the non-shedding event consists of all three components of vorticity, while the shedding event is dominated by the azimuthal vorticity component (ω_θ^*). This observation is further checked for all the timescale events by computing the probability of time duration of events for which the radial and spanwise vorticity components are zero (i.e., $|\boldsymbol{\omega}^*|_{rz} \approx 10^{-3}$, where, $|\boldsymbol{\omega}^*|_{rz} = \sqrt{\omega_r^{*2} + \omega_z^{*2}}$), and the result is presented in figure 24c. This plot clearly shows that the probability of dominating azimuthal component is maximum for the shedding events, and this probability decreases for increasing time-scales. The vortical structures generated due to the vertical bars are predominately dominated by the azimuthal component. Now it is surmised that, for the shedding event, these vortical structures move fast and impinge on the cylinder with the same predominance of azimuthal component. On the other hand, the predominance of the azimuthal component is lost for the long non-shedding events. Therefore, we classify the shedding events as the ones that have the timescale which is closer to that of vortex shedding and contain more than 50% dominance of ω_θ^* compared with the other two vorticity components. On the other hand, the non-shedding events are classified as the ones having large timescales and less than 50% dominance of ω_θ^* compared with ω_r^* and ω_z^*. Figure 24c also shows that more than 75% of the effective timescale range (i.e. $\tau_{min} < \tau < 0.75\tau_{2(opt)}$) is occupied by azimuthally dominated events (which also happen to be the shedding events). At the same time, there is also some contribution to the effective timescale range from the non-shedding events although the probability of such events is less compared with
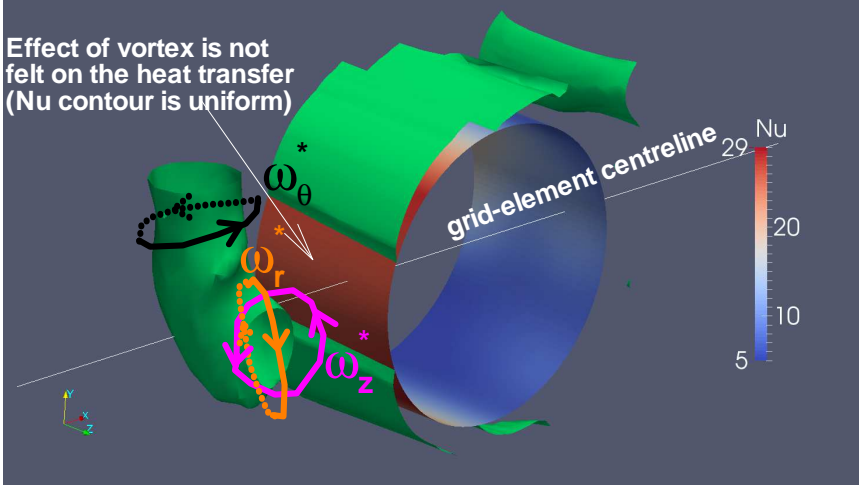
(a)
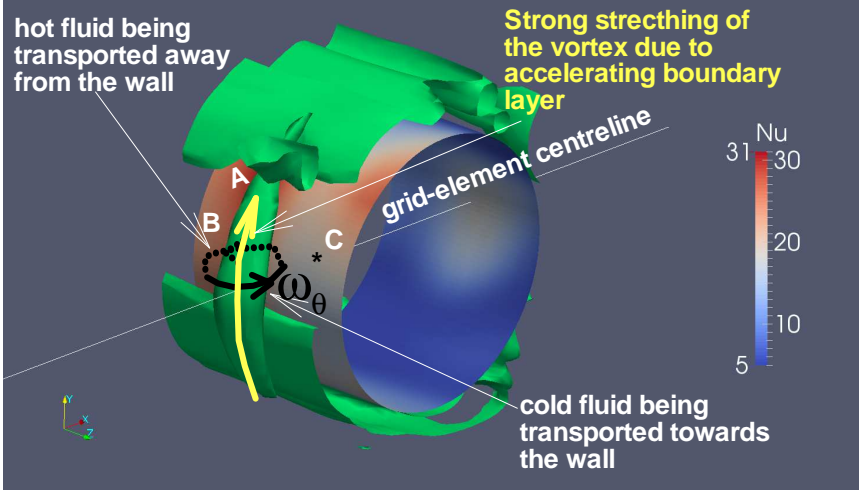
(b)

Figure 25: Typical vortical structures of a non-shedding event: (a) While approaching the cylinder (b) After been stretched by the mean boundary layer. The 3D region plotted in this figure has the dimensions of $-1 \leqslant y/D \leqslant 1$, $-1 \leqslant z/D \leqslant 1$ and $-1 \leqslant x_c/D \leqslant 1$

the shedding events (see figure 22d). In summary, the turbulent events of timescale $\tau < 0.75\tau_{2(opt)}$ are the shedding events which have frequencies closer to ϕ_λ and are dominated by azimuthal vortical structures. On the other hand, the turbulent events for which $\tau > 0.75\tau_{2(opt)}$ represent the non-shedding events whose frequencies are much higher than ϕ_λ and contain all vorticity components in their vortical structures.

While we established that much of the heat transfer in the production case is due to azimuthal vortical flow, the underlying mechanism remains unclear. Analysing how vor-

tical structures transfer heat from the cylinder surface can shed light to this mechanism. We also compare our mechanism with that of Hubble *et al.* (2013). As mentioned earlier, the heat transfer in the production case is mostly due to shedding events, with small contribution from the non-shedding events (i.e. $\tau_{min} < \tau < \tau_{2(opt)}$). The heat transfer mechanism for the non-shedding events is addressed first as it is similar to the one found in the literature. It was shown that the structures for the non-shedding events have all three vorticity components. Let us consider a turbulent event having a timescale greater than $\tau_{2(opt)}$.
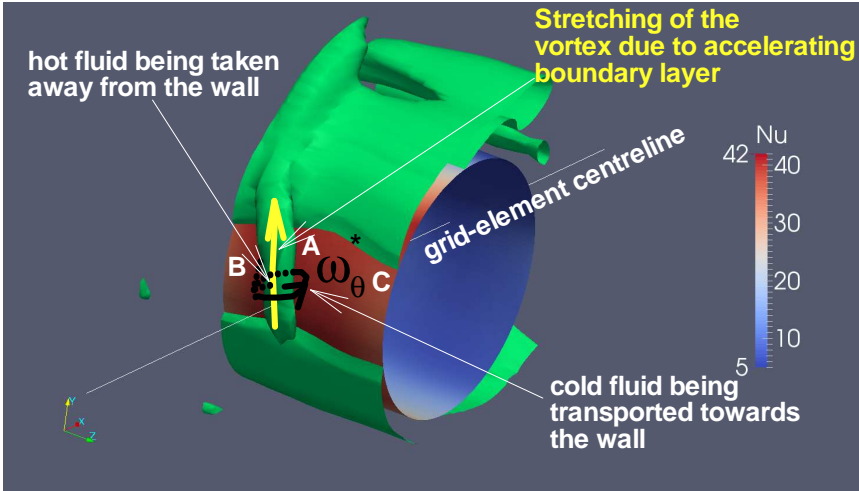
A typical vortical structure approaching the cylinder in this non-shedding event is shown in figure 25a. This vortical structure does not leave a footprint on the surface, even as it approaches the cylinder, so the Nu contour on the wall is almost uniform (figure 25a). This result closely resembles that of Hubble *et al.* (2013) where it was reported that the proximity of the vortex influences the heat transfer. In figure 25a, the vortex is relatively far from the cylinder surface compared with figure 25b, and thus its effectiveness on heat transfer is limited. Once the vortical structure comes closer to the cylinder, it is stretched by the action of the accelerating boundary layer, the effect is felt on the surface; notice the larger Nu in the location where the vortex lies (denoted as 'A' in figure 25b), and smaller Nu in other locations (points 'B' and 'C' in figure 25b). This again validates the mechanism of Hubble *et al.* (2013) that the vortex has a considerable role in heat transfer when it is very close to the surface. They also reported that the vorticity magnitude of the oncoming vortex increases when it approaches the cylinder. This also found to be valid in our case as figure 24b shows increase in vorticity magnitude during the approach process (i.e. from $tU_{inc}/D=$ 2550 to 2570). However, it is extremely difficult to measure vortex size and circulation in 3D flows, and therefore, the influence of these parameters are not discussed here. Yet, one can apply the Taylor hypothesis to the time-scale events and can conclude that the large vortical structures are of little importance in heat transfer enhancement.

In summary, in the case of non-shedding events, the oncoming vortex does not contribute much to heat transfer, unless it is stretched by the accelerating boundary layer. Note also that the vortex is stretched in the azimuthal direction causing an increase in azimuthal vorticity while reducing the other two components. Due to this, the free-stream cold fluid is transported towards the cylinder, and the hot fluid from the surface is transported away. The aforementioned stretching mechanism by the boundary layer is similar to the hypothesis proposed by Hunt (1973) based on rapid distortion theory, and it is similar to the one observed in the simulations of Wissink & Rodi (2006); Xiong & Lele (2007); Bhaskaran & Lele (2010).

Attention is now turned to the heat transfer mechanism for the shedding events which have more than 50% of ω_θ dominance (i.e. $\tau < 0.75\tau_{2(opt)}$). A typical vortical structure of a shedding event approaching the cylinder is depicted in figure 26a. An interesting observation can be made. The heat transfer on the cylinder is clearly affected by the presence of the vortex even before this is stretched by the accelerating boundary layer. The Nu contour on the cylinder wall is not uniform, and the largest values align with the vortex direction (point 'A' in figure 26a) and the smallest values are on the flanks of the vortex (points 'B' and 'C'). This can be attributed to the fact that the azimuthal vortex transports fluid perpendicular to the cylinder surface causing an effective heat transfer from the cylinder. This mechanism is similar to the one observed for the vortex-ring-wall-interaction in the experimental study of Hubble *et al.* (2013). Here, the stagnation point always feels the effect of down-wash as the approaching vortex is azimuthally dominant. The effectiveness of this vortex is further increased when the mean accelerating flow acts on it (by means of stretching) along the cylinder surface as seen in figure 26a. This
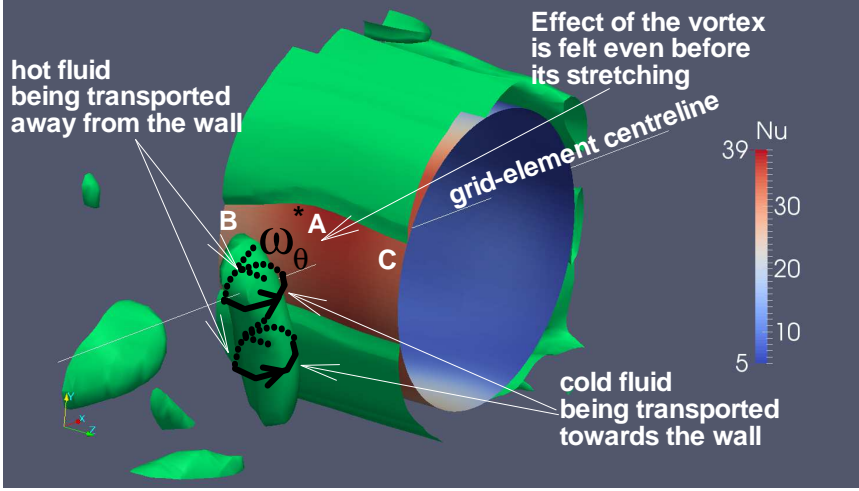
(a)

(b)

Figure 26: Typical vortical structures of a shedding event: (a) While approaching the cylinder (b) After been stretched by the mean boundary layer. The 3D region plotted in this figure has the dimensions of $-1 \leqslant y/D \leqslant 1$, $-1 \leqslant z/D \leqslant 1$ and $-1 \leqslant x_c/D \leqslant 1$

stretching increases further the azimuthal vortical strength causing even higher heat transfer in areas that align with the vortex (point 'A' in figure 26b). This heat transfer mechanism is different to the previously noted mechanism for the non-shedding event as the approaching vortex contributes to heat transfer even before it gets stretched.

Therefore, the shedding events, which consist of a dominant azimuthal vortical component, increase heat transfer even without the help of the mean accelerating flow. In this respect, turbulence in the production case is unique: firstly the boundary layer is

receptive to the shedding frequency, and secondly the flow is dominated by shedding events that carry mostly azimuthal vorticity that is very effective in transferring heat. These characteristics explain why the production case has much higher heat transfer rate than the decay case although the oncoming turbulent intensities are similar.

We also extended this timescale analysis to the production case at $z/D = \pm 5$ and the peak case. We noted that the intermittency level decreases for both the cases, and thus the number of shedding events is smaller when performing the timescale separation analysis. Yet, we observed once again that the shedding events have higher heat transfer due to their azimuthal vorticity dominance. Therefore, the results presented in this subsection is also applicable for the production case at $z/D = \pm 5$ and the peak case. In these two cases, the heat transfer is because of the dominance of azimuthal vorticity component associated with the shedding events combined with higher turbulent intensity. On the other hand, the timescale separation analysis is not applicable to the decay case as it is fully turbulent and $|\boldsymbol{\omega}^*_{th}|$ can not be determined. However, the heat transfer mechanism discussed for the non-shedding event is valid for the decay case. This is the same mechanism also reported in the literature.

9. Comparison with high Reynolds number experiments

In this section, the observations of this DNS study are compared with the experimental study of Melina *et al.* (2017). The lowest Reynolds number of these experiments is $Re_D = 11,100$. Two significant differences are noted: first the decay region of the experiment was observed to have higher heat transfer than the production region, although the locations examined in both the regions had approximately similar turbulent intensity. Secondly, the maximum heat transfer coefficient was observed at the front stagnation point unlike the shift of approximately 45° observed in this DNS study. These two differences are explained below.

Regarding the heat transfer rates in the decay and production cases, equation (7.1) predicts that the value of ϕ_λ scales with the square root of Reynolds number. It appears that in the high Reynolds numbers experiment of Melina *et al.* (2017), the dominant frequency is higher and is located in an area of the spectrum that is less energetic. Therefore in the experiments, the characteristics of turbulence in the production case are not as effective compared to the present low Reynolds number DNS, and that is why the production case exhibits lower heat transfer than the decay case.

The second difference can also be explained based on the dominant frequency concept and figures 17. Notice in figure 17a that the shift in $\langle Nu \rangle_{max}$ is more prominent only along the grid-element centreline where the dominant frequency of the fluctuations are more energetic. Along the bar-centreline, where the oncoming turbulent intensity is much higher, the shift in $\langle Nu \rangle_{max}$ is less prominent. Turbulent intensity increases along the azimuthal direction from the front stagnation point to a certain angle due to the presence of the grid-element bars for the production case (see figure 8). Due to higher values of turbulent intensity along with an energetic dominant frequency, $\langle Nu \rangle_{max}$ is shifted by 45° from the front stagnation point. On the other hand, in the experiments, although the turbulent intensity also increases along the azimuthal direction from the front stagnation point, this increase becomes less effective as the laminar boundary layer is not receptive. Due to this, the experiments (as well the bar-centreline of the simulations) have a near-constant or a slow decay of $\langle Nu \rangle$ from the front stagnation point to 45°.

10. Conclusions

This paper presented the first ever DNS study devoted to the investigation of the effect of different regions in the wake of grid-element on the heat transfer from a circular cylinder. Unlike previous studies, this paper has a single square grid-element to generate turbulence upstream of the cylinder. Due to the fine resolution requirements for the grid-element and cylinder, the simulations have been carried out for small Reynolds number. The cylinder is placed at three distinct locations downstream of the grid-element namely the production, peak, and decay regions. In order to make meaningful comparisons between these regions, the turbulent intensity of the production and decay regions is kept similar. The peak case has the highest turbulent intensity of 15%, while the production and peak cases have a turbulent intensity of 11%.

The oncoming turbulence in the production, and peak regions is identified to have the following characteristics: non-*Gaussian*, inhomogeneous, and intermittent. On the other hand, the turbulence in the decay region is *Gaussian*, homogeneous and fully turbulent.

There are three important take-away results from this study. The first is related to the heat transfer rate between different regions of grid-element. It is established that the production region has the highest heat transfer increase although its turbulent intensity is the same as that of the decay region. The second important result is on the existing stagnation point heat transfer correlations. It was found that the production and peak turbulence cases do not satisfy the existing correlations, but the decay case does fulfill the correlation. Note that this is the first DNS study that reports invalidity of such correlations. The final important finding concerns the maximum heat transfer on the surface of the cylinder. It is found that the maximum occurs around 45° away from the front stagnation point even in the decay case where the turbulence is nearly homogeneous.

We explored why the production and peak turbulence cases have different heat transfer increase compared to the previously reported studies. It is found that the turbulence in the production and peak regions is unique, in the sense that the dominant boundary layer frequency (ϕ_λ) lies closer to the vortex shedding frequency. This makes the boundary layer very susceptible to the impinging disturbances. Besides this, the flow is dominated by short timescale shedding events (i.e turbulent events where $\tau < 0.75\tau_{2(opt)}$) that have timescales of the order of shedding timescale. These shedding events mainly carry azimuthal vorticity, which increases the heat transfer even before it is stretched by the mean accelerating boundary layer. These two unique characteristics results in very high increase of heat transfer, thus making the existing stagnation point heat transfer correlations invalid for the production and peak regions.

The answer for why the maximum heat transfer is shifted away from the front stagnation point is explored through statistical analysis of Nusselt number. Our results show that additional intense events occur at the maximum heat transfer point compared to the front stagnation point. It is believed that the presence of the grid-element bars gives rise to occurrence of such additional intense events.

As a final comment, our DNS provides evidence of different heat transfer enhancement when fluctuations with the same turbulent intensity have different spectral content. We suggest that in order to gain maximum increase in heat transfer, the flow should be tuned so that the fluctuating energy is concentrated in the frequency band that maximises the receptivity of the boundary layer developing in the solid body. This result can be exploited for engineering applications such as optimal extraction of heat transfer in a heat-exchanger.

Acknowledgments

REFERENCES

AMES, FE 1991 Heat transfer with high intensity, large scale turbulence: the flat plate turbulent boundary layer and the cylindrical stagnation point. In *Dept. Mech. Engg. Rep.*, pp. HMT–44. Stanford University, Stanford, CA.

AMES, FE 1995 The influence of large scale high intensity turbulence on vane heat transfer. In *ASME 1995 International Gas Turbine and Aeroengine Congress and Exposition*, pp. V004T09A021–V004T09A021. American Society of Mechanical Engineers.

AMES, FE, WANG, C & BARBOT, PA 2002 Measurement and prediction of the influence of catalytic and dry low NOx combustor turbulence on vane surface heat transfer. In *ASME Turbo Expo 2002: Power for Land, Sea, and Air*, pp. 969–980. American Society of Mechanical Engineers.

BALAY, S, ABHYANKAR, S, ADAMS, M, BROWN, J, BRUNE, P, BUSCHELMAN, K, EIJKHOUT, V, GROPP, W, KAUSHIK, D, KNEPLEY, M & OTHERS 2014 Petsc users manual revision 3.5. *Tech. Rep.*. Technical report, Argonne National Laboratory (ANL).

BHASKARAN, R & LELE, SK 2010 Large eddy simulation of free-stream turbulence effects on heat transfer to a high-pressure turbine cascade. *J. Turbul.* **11**, 1–15.

BISSET, DK, HUNT, JCR & ROGERS, MM 2002 The turbulent/non-turbulent interface bounding a far wake. *J. Fluid Mech.* **451**, 383–410.

CHOWDHURY, N & AMES, FE 2013 The response of high intensity turbulence in the presence of large stagnation regions. In *ASME Turbo Expo 2013: Turbine Technical Conference and Exposition*, pp. V03CT14A020–V03CT14A020. American Society of Mechanical Engineers.

DIMOPOULOS, HG & HANRATTY, TJ 1968 Velocity gradients at the wall for flow around a cylinder for Reynolds numbers between 60 and 360. *J. Fluid Mech.* **33** (02), 303–319.

DULLENKOPF, K & MAYLE, RE 1994 The effects of incident turbulence and moving wakes on laminar heat transfer in gas turbines. *ASME J. Turbomach.* **116** (1), 23–28.

DULLENKOPF, K & MAYLE, RE 1995 An account of free-stream-turbulence length scale on laminar heat transfer. *ASME J. Turbomach.* **117** (3), 401–406.

DULLENKOPF, K, SCHULZ, A & WITTIG, S 1990 The effect of incident wake conditions on the mean heat transfer of an airfoil. In *ASME 1990 International Gas Turbine and Aeroengine Congress and Exposition*, pp. V004T09A023–V004T09A023. American Society of Mechanical Engineers.

ECKERT, ERG 1952 Distribution of heat-transfer coefficients around circular cylinders in crossflow at Reynolds numbers from 20 to 500. *Trans. ASME* **74**, 343–347.

GOMES-FERNANDES, R, GANAPATHISUBRAMANI, B & VASSILICOS, JC 2012 Particle image velocimetry study of fractal-generated turbulence. *J. Fluid Mech.* **711**, 306–336.

HUBBLE, DO, VLACHOS, PP & DILLER, TE 2013 The role of large-scale vortical structures in transient convective heat transfer augmentation. *J. Fluid Mech.* **718**, 89–115.

HUNT, JCR 1973 A theory of turbulent flow round two-dimensional bluff bodies. *J. Fluid Mech.* **61** (04), 625–706.

JONES, WP & LAUNDER, BE 1973 The calculation of low-Reynolds-number phenomena with a two-equation model of turbulence. *Int. J. Heat Mass Transfer.* **16** (6), 1119–1130.

JUNKHAN, GH & SEROVY, GK 1967 Effects of free-stream turbulence and pressure gradient on flat-plate boundary-layer velocity profiles and on heat transfer. *ASME J. Heat Transfer* **89** (2), 169–175.

KESTIN, J, MAEDER, PF & WANG, HE 1961 Influence of turbulence on the transfer of heat from plates with and without a pressure gradient. *Intl J. Heat Mass Transfer* **3** (2), 133–154.

KINGERY, JE & AMES, FE 2016 Stagnation region heat transfer augmentation at very high turbulence levels. *ASME J. Turbomach.* **138** (8), 081005.

KRALL, KM & ECKERT, ERG 1973 Local heat transfer around a cylinder at low Reynolds number. *ASME J. Heat Transfer* **95** (2), 273–275.

LAIZET, S, NEDIĆ, J & VASSILICOS, JC 2015 Influence of the spatial resolution on fine-scale features in DNS of turbulence generated by a single square grid. *Int. J. Comput. Fluid D.* **29** (3-5), 286–302.

LIU, X & RODI, W 1994 Surface pressure and heat transfer measurements in a turbine cascade with unsteady oncoming wakes. *Exp. Fluids* **17** (3), 171–178.

LOWERY, GW & VACHON, RI 1975 The effect of turbulence on heat transfer from heated cylinders. *Intl J. Heat Mass Transfer* **18** (11), 1229–1242.

MAGARI, PJ & LAGRAFF, LE 1994 Wake-induced unsteady stagnation-region heat transfer measurements. *ASME J. Turbomach.* **116** (1), 29–38.

MAZELLIER, N & VASSILICOS, JC 2010 Turbulence without Richardson–Kolmogorov cascade. *Phys. Fluids* **22** (7), 075101.

MELINA, G, BRUCE, PJK, HEWITT, GF & VASSILICOS, JC 2017 Heat transfer in production and decay regions of grid-generated turbulence. *Intl. J. Heat Mass Transfer* **109**, 537–554.

PAUL, I 2017 Evolution of velocity and scalar gradients in a spatially developing turbulence. PhD thesis, Imperial College London UK.

PAUL, I, PAPADAKIS, G & VASSILICOS, JC 2017 Genesis and evolution of velocity gradients in near-field spatially developing turbulence. *J. Fluid Mech.* **815**, 295–332.

PAUL, I, PAPADAKIS, G & VASSILICOS, JC 2018 Evolution of passive scalar statistics in a spatially developing turbulence. *Phys. Rev. Fluids* **3** (1), 014612.

PAUL, I, PRAKASH, KA, VENGADESAN, S & PULLETIKURTHI, V 2016 Analysis and characterisation of momentum and thermal wakes of elliptic cylinders. *J. Fluid Mech.* **807**, 303–323.

PAXSON, DE & MAYLE, RE 1991 Laminar boundary layer interaction with an unsteady passing wake. *ASME J. Turbomach.* **113** (3), 419–427.

SCHLICHTING, H & GERSTEN, K 2016 *Boundary-layer theory*. Springer.

SEOUD, RE & VASSILICOS, JC 2007 Dissipation and decay of fractal-generated turbulence. *Phys. Fluids* **19** (10), 105108.

SON, JS & HANRATTY, TJ 1969 Numerical solution for the flow around a cylinder at Reynolds numbers of 40, 200 and 500. *J. Fluid Mech.* **35** (02), 369–386.

TAVEIRA, RR, DIOGO, JS, LOPES, DC & DA SILVA, CB 2013 Lagrangian statistics across the turbulent-nonturbulent interface in a turbulent plane jet. *Phys. Rev. E* **88** (4), 043001.

VALENTE, PC & VASSILICOS, JC 2011 The decay of turbulence generated by a class of multiscale grids. *J. Fluid Mech.* **687**, 300–340.

VAN FOSSEN, GJ, SIMONEAU, RJ & CHING, CY 1995 Influence of turbulence parameters, Reynolds number, and body shape on stagnation-region heat transfer. *J. Heat Transfer* **117** (3), 597–603.

VANFOSSEN, GJ & SIMONEAU, RJ 1987 A study of the relationship between free-stream turbulence and stagnation region heat transfer. *J. Heat Transfer* **109** (1), 10–15.

VASSILICOS, JC 2015 Dissipation in turbulent flows. *Annu. Rev. Fluid Mech.* **47**, 95–114.

VENEMA, L, VON TERZI, D, BAUER, H-J & RODI, W 2011 DNS of heat transfer increase in a cylinder stagnation region due to wake-induced turbulence. *Intl J. Heat Fluid Flow* **32** (3), 492–498.

VENEMA, L, VON TERZI, D, BAUER, H-J & RODI, W 2014 Direct numerical simulation of stagnation point heat transfer affected by varying wake-induced turbulence. *ASME J. Turbomach.* **136** (2), 021008.

WATANABE, T, SAKAI, Y, NAGATA, K, ITO, Y & HAYASE, T 2014 Vortex stretching and compression near the turbulent/non-turbulent interface in a planar jet. *J. Fluid Mech.* **758**, 754–785.

WISSINK, JG & RODI, W 2006 Direct numerical simulation of flow and heat transfer in a turbine cascade with incoming wakes. *J. Fluid Mech.* **569**, 209–247.

WISSINK, JG & RODI, W 2009 DNS of heat transfer in transitional, accelerated boundary layer

flow over a flat plate affected by free-stream fluctuations. *Intl J. Heat Fluid Flow* **30** (5), 930–938.

WISSINK, JG & RODI, W 2011*a* Direct numerical simulation of heat transfer from the stagnation region of a heated cylinder affected by an impinging wake. *J. Fluid Mech.* **669**, 64–89.

WISSINK, JG & RODI, W 2011*b* Heat transfer from the stagnation area of a heated cylinder at Re_D=140,000 affected by free-stream turbulence. *Intl J. Heat Mass Transfer* **54** (11), 2535–2541.

XIONG, Z & LELE, SK 2004 Distortion of upstream disturbances in a Hiemenz boundary layer. *J. Fluid Mech.* **519**, 201–232.

XIONG, Z & LELE, SK 2007 Stagnation-point flow under free-stream turbulence. *J. Fluid Mech.* **590**, 1–33.

YARDI, NR & SUKHATME, SP 1978 Effects of turbulence intensity and integral length scale of a turbulent free stream on forced convection heat transfer from a circular cylinder in cross flow. In *6th International Heat Transfer Conference, Volume 5* , , vol. 5, pp. 347–352.

ZDRAVKOVICH, MM 1997 *Flow around Circular Cylinders: Volume 1: Fundamentals* , , vol. 1. Oxford University Press.

ZHOU, Y, NAGATA, K, SAKAI, Y, ITO, Y & HAYASE, T 2016*a* Enstrophy production and dissipation in developing grid-generated turbulence. *Phys. Fluids* **28** (2), 025113.

ZHOU, Y, NAGATA, K, SAKAI, Y, ITO, Y & HAYASE, T 2016*b* Spatial evolution of the helical behavior and the 2/3 power-law in single-square-grid-generated turbulence. *Fluid Dyn. Res.* **48** (2), 021404.

ZHOU, Y, NAGATA, K, SAKAI, Y, SUZUKI, H, ITO, Y, TERASHIMA, O & HAYASE, T 2014 Development of turbulence behind the single square grid. *Phys. Fluids* **26** (4), 045102.

ZHOU, Y & VASSILICOS, JC 2017 Related self-similar statistics of the turbulent/non-turbulent interface and the turbulence dissipation. *J. Fluid Mech.* **821**, 440–457.